The Astrophysical Journal Supplement Series, 244:35 (21pp), 2019 October https://doi.org/10.3847/1538-4365/ab4258

A Census of Early-phase High-mass Star Formation in the Central Molecular Zone

Xing Lu (吕行)[1], Elisabeth A. C. Mills[2], Adam Ginsburg[3], Daniel L. Walker[1,4], Ashley T. Barnes[5], Natalie Butterfield[6], Jonathan D. Henshaw[7], Cara Battersby[8], J. M. Diederik Kruijssen[9], Steven N. Longmore[10], Qizhou Zhang[11], John Bally[12], Jens Kauffmann[13], Jürgen Ott[3], Matthew Rickert[3,14], and Ke Wang[15]
[1] National Astronomical Observatory of Japan, 2-21-1 Osawa, Mitaka, Tokyo, 181-8588, Japan; xinglv.nju@gmail.com, xing.lu@nao.ac.jp
[2] Physics Department, Brandeis University, 415 South Street, Waltham, MA 02453, USA
[3] National Radio Astronomy Observatory, 1003 Lopezville Road, Socorro, NM 87801, USA
[4] Joint ALMA Observatory, Alonso de Córdova 3107, Vitacura 763 0355, Santiago, Chile
[5] Argelander-Institut für Astronomie, Universität Bonn, Auf dem Hügel 71, D-53121 Bonn, Germany
[6] Green Bank Observatory, 155 Observatory Road, P.O. Box 2, Green Bank, WV 24944, USA
[7] Max-Planck-Institut für Astronomie, Königstuhl 17, D-69117 Heidelberg, Germany
[8] University of Connecticut, Department of Physics, 2152 Hillside Road, Storrs, CT 06269, USA
[9] Astronomisches Rechen-Institut, Zentrum für Astronomie der Universität Heidelberg, Mönchhofstraße 12-14, D-69120 Heidelberg, Germany
[10] Astrophysics Research Institute, Liverpool John Moores University, 146 Brownlow Hill, Liverpool L3 5RF, UK
[11] Center for Astrophysics, Harvard & Smithsonian, 60 Garden Street, Cambridge, MA 02138, USA
[12] Department of Astrophysical and Planetary Sciences, University of Colorado, 389 UCB, Boulder, CO 80309, USA
[13] Haystack Observatory, Massachusetts Institute of Technology, Westford, MA 01886, USA
[14] CIERA and Department of Physics and Astronomy, Northwestern University, 2145 Sheridan Road, Evanston, IL 60208-3112, USA
[15] Kavli Institute for Astronomy and Astrophysics, Peking University, 5 Yiheyuan Road, Haidian District, Beijing 100871, People's Republic of China
Received 2019 August 17; revised 2019 August 31; accepted 2019 September 5; published 2019 October 14

Abstract

We present new observations of the *C*-band continuum emission and masers to assess high-mass ($>8\,M_{\odot}$) star formation at early evolutionary phases in the inner 200 pc of the Central Molecular Zone (CMZ) of the Galaxy. The continuum observation is complete to free–free emission from stars above 10–11 $M_{\odot}$ in 91% of the covered area. We identify 104 compact sources in the continuum emission, among which five are confirmed ultracompact H II regions, 12 are candidates of ultracompact H II regions, and the remaining 87 sources are mostly massive stars in clusters, field stars, evolved stars, pulsars, extragalactic sources, or of unknown nature that is to be investigated. We detect class II CH_3OH masers at 23 positions, among which six are new detections. We confirm six known H_2CO masers in two high-mass star-forming regions and detect two new H_2CO masers toward the Sgr C cloud, making it the ninth region in the Galaxy that contains masers of this type. In spite of these detections, we find that current high-mass star formation in the inner CMZ is only taking place in seven isolated clouds. The results suggest that star formation at early evolutionary phases in the CMZ is about 10 times less efficient than expected from the dense gas star formation relation, which is in line with previous studies that focus on more evolved phases of star formation. This means that if there will be any impending, next burst of star formation in the CMZ, it has not yet begun.

Unified Astronomy Thesaurus concepts: Star formation (1569); Galactic center (565); H II regions (694); Astrophysical masers (103)

1. Introduction

Observations toward the Central Molecular Zone (CMZ), the inner ∼500 pc of the Galaxy, suggest a large amount of molecular gas ($>10^7\,M_{\odot}$, mean density $\sim 10^4\,\mathrm{cm}^{-3}$; Bally et al. 1987; Longmore et al. 2013a). However, the measured star formation rate (SFR) in the CMZ is about 10 times lower than expected from the dense gas star formation relation extrapolated from the nearby molecular clouds (Yusef-Zadeh et al. 2009; An et al. 2011; Immer et al. 2012b; Longmore et al. 2013a; Barnes et al. 2017). Various mechanisms (or combinations of them) have been suggested to explain the inefficient star formation in the CMZ, including inhibition of gas collapse by strong turbulence (Kruijssen et al. 2014; Dale et al. 2019), episodic star formation regulated by Galactic dynamics (Kruijssen et al. 2014; Krumholz & Kruijssen 2015; Krumholz et al. 2017; Meidt et al. 2018; Kruijssen et al. 2019), and higher density thresholds for star formation (Kruijssen et al. 2014; Federrath et al. 2016; Krumholz et al. 2017).

Despite the advances in theoretical models, star formation in the CMZ is not well-characterized observationally. Previous studies have used infrared luminosities or young stellar objects (YSOs) in infrared bands of the CMZ to measure star formation (e.g., Yusef-Zadeh et al. 2009; An et al. 2011; Immer et al. 2012b; Barnes et al. 2017). However, these approaches suffer from heavy extinction in the infrared bands toward the Galactic Center (Barnes et al. 2017) and contamination from more evolved stellar populations (Koepferl et al. 2015). More recently, star formation in a few clouds in the CMZ was characterized at high angular resolution by using masers and ultracompact (UC) H II regions (Lu et al. 2015, 2019; Kauffmann et al. 2017a), which are free of extinction and trace early-phase high-mass ($>8\,M_{\odot}$) star formation. A few CMZ-wide surveys of masers have also provided important information on the distribution of star formation in the CMZ (e.g., Caswell et al. 2010; Chambers et al. 2014; Cotton & Yusef-Zadeh 2016; Rickert et al. 2019).

Here we report high-angular-resolution, high-sensitivity observations of the *C*-band line and continuum emission toward the inner CMZ carried out with the NRAO[16] Karl G. Jansky Very Large Array (VLA). Our observations feature a large

[16] The National Radio Astronomy Observatory is a facility of the National Science Foundation operated under cooperative agreement by Associated Universities, Inc.

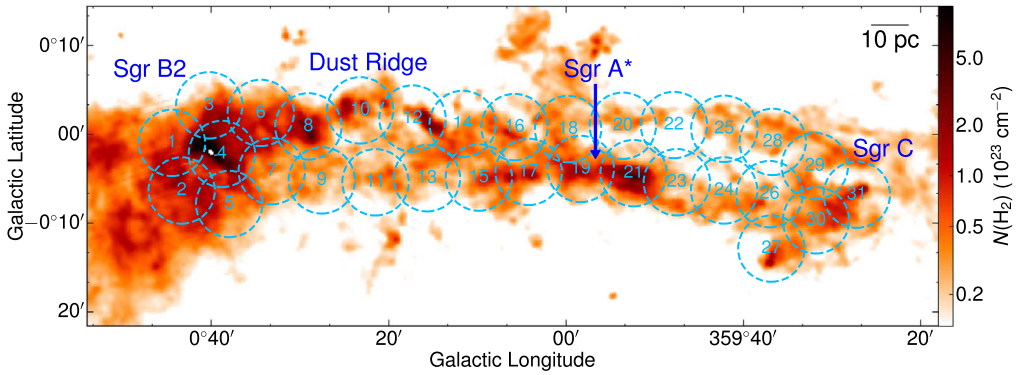

Figure 1. Spatial coverage of the VLA observations. Cyan dashed circles show the fields, with field indices marked at the circle centers. The position of Sgr A* is marked by an arrow, while approximate locations of the other three tiles (Sgr B2, Dust Ridge, Sgr C) are labeled. The background image shows molecular gas column densities derived from *Herschel* (Battersby et al. 2011).

Table 1
Summary of VLA Observations

Obs. Date	Field Indices[a]	No. of Unflagged Antennas	*uv* distance ($k\lambda$)	Calibrators[b]
2016 Aug 21	8–17, 19, 21	23	2–230	3C 286, J1744−3116
2016 Sep 12	18, 20, 22–31	23	2–253	3C 286, J1744−3116
2016 Oct 4	1–7	25	4–472	3C 286, J1744−3116

Notes.
[a] Field indices are marked in Figure 1.
[b] Bandpass/flux calibrator and phase calibrator, respectively.

surveyed area combined with high resolution, which enables a comprehensive census of masers and UC H II regions. We aim to study high-mass star formation at early evolutionary phases, in which protostars are deeply embedded in molecular gas and dust, when near- to mid-infrared emission from star formation is weak due to absorption. Therefore, they are best traced by masers and free–free emission from embedded UC H II regions. In Section 2, we introduce our observations. In Section 3, we report maser and continuum source detections, and specifically, the detection of several new masers toward high-mass star-forming regions. Then, in Section 4, we identify candidates of UC H II regions from the continuum emission and discuss the implications for star formation in the CMZ. We conclude and summarize our findings in Section 5. Throughout this paper, we adopt a distance of 8.1 kpc to the CMZ (Gravity Collaboration et al. 2018).

2. Observations and Data Reduction

The VLA observations were carried out in the B configuration in 2016 August–October with the project code 16A–173. A brief summary of the observations is shown in Table 1. The *C*-band receiver was used to cover six lines, including two CH_3OH lines at the rest frequencies of 6.668 GHz and 5.005 GHz, a radio recombination line H(111)α at the rest frequency of 4.744 GHz, and three formaldehyde isotopolog lines H_2CO, $H_2\,^{13}CO$, and $H_2C^{18}O$ between rest frequencies of 4.389 and 4.830 GHz. For each line, a velocity range of $\pm 200\,km\,s^{-1}$was covered. In addition to the lines, a total of 16 wideband spectral windows were used to cover a 2 GHz wide continuum between 4.2 and 6.9 GHz, but owing to strong radio frequency interference (RFI), the available bandwidth for continuum imaging is less, with a typical value of 1.7 GHz.

We targeted the inner 200 pc of the CMZ (Figure 1), where high-mass stars are most likely to be forming given the high gas column densities (Kauffmann & Pillai 2010). A total of 31 fields were observed. The fields are not Nyquist-sampled, as we do not target extended structures above the largest recoverable angular scale of $\sim 1'$; therefore, mosaicked imaging is not required. Among these fields, seven were used to cover the Sgr B2 region in a hexagonal pattern (fields 1–7), and the others were used to cover the high column density ($\gtrsim 10^{23}\,cm^{-2}$) regions roughly along the ring-like 100 pc structure seen in *Herschel* infrared emission images (Molinari et al. 2010). Each field was integrated for about 3.5 minutes in snapshot mode. The FWHM size of the primary beam of the VLA at the central frequency of 5.56 GHz is $7\farcm5$, and this size varies from $8'$ to $7'$ from the lowest to the highest observed frequencies.

We calibrated the data following standard procedures using CASA 5.4.0. Note that at this frequency band, significant RFI exists.[17] Therefore, we first used the rflag algorithm implemented in CASA to automatically identify and flag RFI in the calibrators, then performed a manual flagging to remove any other significant RFI.

Then we imaged the lines and continuum using CASA 5.4.0. For the primary target line, the CH_3OH line at 6.668 GHz, we first performed Hanning smoothing to merge every two velocity channels in the calibrated data, in order to remove the effects of Gibbs ringing. The resulting channel width is $0.35\,km\,s^{-1}$. We used the uvcontsub task in CASA to subtract the continuum. Then we imaged each field separately using the tclean task, with the Briggs weighting and a robust number of 0.5. When there is a strong maser detected in the field, we performed self-calibration using its peak channel and applied the calibration tables to all

[17] https://science.nrao.edu/facilities/vla/docs/manuals/obsguide/rfi

Table 2
Comparison of CMZ Radio Continuum Surveys

	Band/Frequency	Resolution	Sensitivity[a]
This work	*C*-band/5.56 GHz	1″	0.025–0.5 mJy beam^{-1}
Becker et al. (1994)	*C*-band/4.9 GHz	4″	⩾2.5 mJy beam^{-1}
Zoonematkermani et al. (1990)	*L*-band/1.4 GHz	5″	⩾1–2 mJy beam^{-1}
Yusef-Zadeh et al. (2004)	*L*-band/1.4 GHz	10″	⩾0.16 mJy beam^{-1}
Lazio & Cordes (2008)	*L*-band/1.4 GHz	2″	⩾0.05 mJy beam^{-1}
Lang et al. (2010)	*L*-band/1.4 GHz	15″	3–4 mJy beam^{-1}

Note.
[a] Lower limits of sensitivities are noted with "⩾." Real noise levels can be at least 10 times higher.

other channels. For the seven fields covering the Sgr B2 region, two antennas were in longer baselines in the array during the observation, which result in a smaller synthesized beam. To get a larger beam size that is consistent with the other fields, we applied *uv* tapering to the seven fields and achieved an image rms of 8 mJy beam^{-1} with a beam size of 1.″2 × 1.″0 in a channel width of 0.35 km s^{-1}. For the other fields, we skipped *uv* tapering and achieved an image rms of 7–9 mJy beam^{-1} with a beam size of 2.″1 × 1.″2 in a channel width of 0.35 km s^{-1}.

Similarly, we imaged the CH_3OH line at 5.005 GHz, the H(111)α line, and the three H_2CO isotopolog lines for each field. Among them, the H_2CO line is more complex: toward several positions in Sgr B2, this line presents deep absorption that extends beyond the velocity coverage of the spectral window (±200 km s^{-1}). This is verified in the wideband spectral window (120 MHz bandwidth) that covers this frequency, where absorption up to ±400 km s^{-1} is found. Therefore, continuum subtraction using the uvcontsub task creates artificial positive intensities for local maxima (less absorption) between deep absorption features. In Section 3.4, we will argue that this does not affect our search for H_2CO masers, but this issue will likely hinder any further investigation of H_2CO absorption toward these positions in Sgr B2 using these data.

Finally, we imaged the continuum emission. We first identified and flagged RFI using the rflag algorithm and then manually flagged any significant residual RFI. As a number of fields contain known extended continuum emission, we used a different imaging strategy than that for the lines. We split the 31 fields into four tiles and mosaicked each one: the first tile mostly covers Sgr B2 and includes fields 1–7; the second tile covers the Dust Ridge (and Sgr B1) and includes fields 8–15; the third tile covers Sgr A and includes fields 16–23; and the fourth tile covers Sgr C and includes fields 24–31. We used the tclean task, with *n*-term of 2, multifrequency synthesis, and multiscale parameters of [0, 3, 10, 30], and gridded the tiles in a cell size of 0.″3. The *n*-term of 2 was used to fit a linear function to the data over a frequency range between 4.2 and 6.9 GHz to obtain the spectral indices α as well as the uncertainty on the fit, $\sigma(\alpha)$. The spectral index α is defined by $S_\nu \propto \nu^\alpha$, where S_ν is the specific flux at the frequency ν. In addition, for the Sgr A and Sgr B2 tiles, where the continuum emission is sufficiently strong, we performed self-calibration to improve the dynamic range, although we found that the signal-to-noise ratio is only improved by a factor of <2, likely because the noise is dominated by partially resolved extended structures. The thermal noise level, 20 μJy beam^{-1}, is not achieved in any of the continuum maps. The measured noise represented by the rms is as low as 25 μJy beam^{-1}toward a few small regions where the continuum emission is undetected (e.g., in the southern part of the Sgr C tile), and as high as 500 μJy beam^{-1} next to Sgr A* and Sgr B2. In Section 3.2, we will construct localized noise maps to account for the varying noise. As a final step, the Stokes-*I* images (with a central frequency at 5.56 GHz), the spectral index images (α), and the spectral index uncertainty images ($\sigma(\alpha)$) were corrected for the primary-beam response using the widebandpbcor task. The continuum images are publicly available at doi:10.5281/zenodo.3361116.

In Table 2, we compare our continuum observation with several radio continuum surveys that have covered the CMZ. Our observation has a higher angular resolution and better sensitivity than the *C*-band continuum survey of Becker et al. (1994), which is part of the Multi-Array Galactic Plane Imaging Survey (MAGPIS), as well as the four *L*-band surveys. The flux of optically thin free–free emission from (UC) H II regions has a weak dependency on the observed frequencies (i.e., a spectral index of −0.1 or slightly higher); therefore, the sensitivities at the different frequencies can be directly compared. It then follows that among the surveys in Table 2, our observations deliver the best sensitivity combined with the highest angular resolution that is optimal for the search of UC H II regions.

To check the quality of the bandpass and flux calibration, we imaged the continuum emission of the phase calibrator, J1744 −3116. This quasar presents a consistent flux of 0.74 Jy across the three epochs of observations and a measured spectral index between −0.03 (the first two epochs) and 0.02 (the last epoch). If the spectral index of the quasar is invariant during the observations, this suggests a systematic uncertainty of 0.05 in the measured spectral indices.

3. Results

In this paper, we focus on potential star formation tracers, including the continuum emission that may arise from H II regions, the class II CH_3OH maser at 6.668 GHz, and the H_2CO maser at 4.830 GHz. The $CH_3OH/H_2CO/H_2$ ^{13}CO absorption, and nonthermal continuum emission will be discussed in forthcoming papers. The CH_3OH line at 5.005 GHz, the H(111) α line, and the $H_2C^{18}O$ line are not detected at the 3σ level.

3.1. C-band Continuum Emission

The *C*-band continuum emission images are presented in Figures 2–5. Bright continuum emission is detected inside the Sgr A (Figure 4) and Sgr B2 (Figure 2) tiles, which results in dynamic-range-limited imaging and significant noise. Nevertheless, we carefully compared with previous observations and found that the well-known features in these two regions are

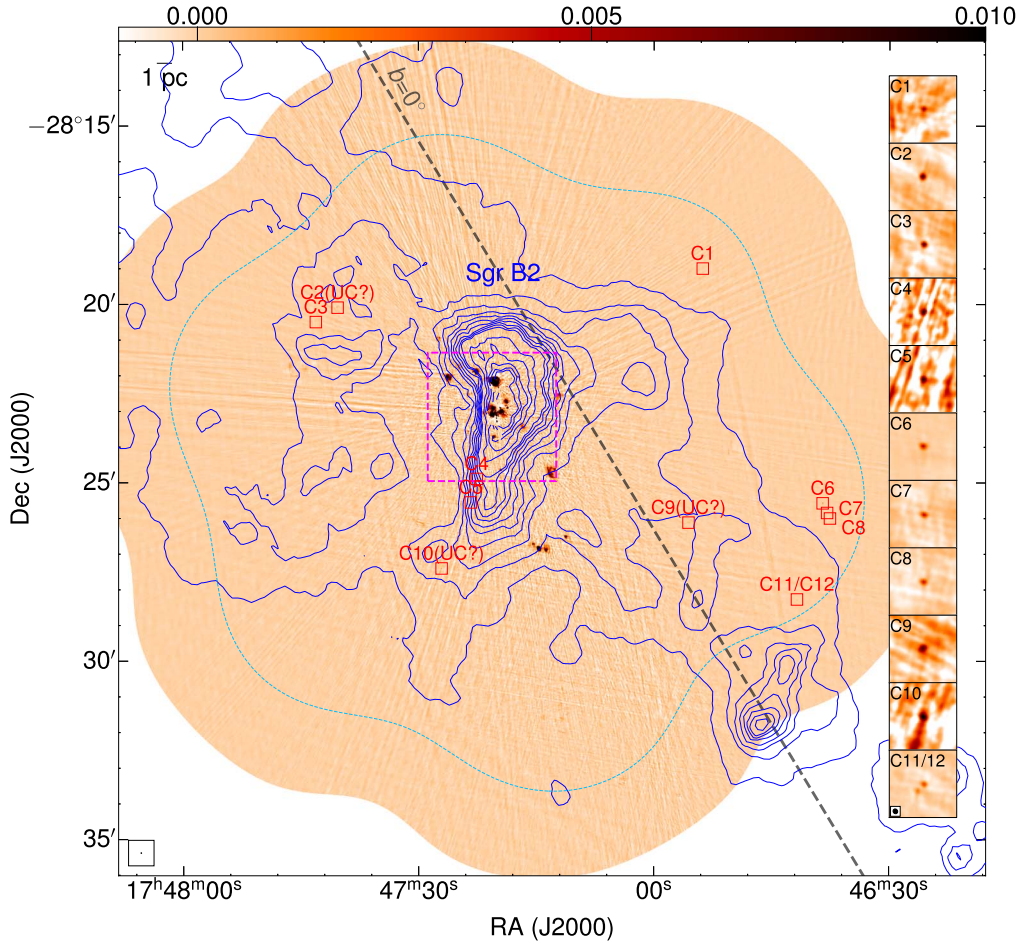

Figure 2. Overview of the Sgr B2 tile. The background image shows the VLA *C*-band continuum emission in the linear scale, which is truncated at an intensity of 0.01 Jy beam^{-1} to highlight faint sources. The unit of the color bar attached to the image top is Jy beam^{-1}. The cyan dashed loop shows the FWHM of the primary beam response of the mosaic. Small boxes mark identified compact sources, among which UC H II candidates and confirmed UC H II regions are labeled with "UC?" and "UC," respectively. Their zoom-in views are shown in the insets aligned on the right. Each inset, centered on the compact source, is 15″ across, and the color scale is adjusted to match the peak intensity of the source. In the last inset (C11/12 in this case), the synthesized beam is plotted in the bottom-left corner. The large dashed box marks the region where masers are detected, and a zoom-in view is in Figure 6. Blue contours show column densities derived from the *Herschel* data (Battersby et al. 2011), between [0.5, 5] × 10^{23} cm^{-2} in steps of 0.5 × 10^{23} cm^{-2}, and then between [5, 15] × 10^{23} cm^{-2} in steps of 2 × 10^{23} cm^{-2}. Names of individual clouds (e.g., Sgr B2 in this tile) are labeled. The dashed diagonal line marks the Galactic latitude line at 0°.

clearly recovered in our images: the mini-spiral arms around Sgr A* (e.g., Ekers et al. 1983; Lo & Claussen 1983; Roberts & Goss 1993; Zhao et al. 2009, 2013, 2016; Tsuboi et al. 2016, 2017); the four H II regions in the Sgr A East region (associated with the 50 km s^{-1} cloud; e.g., Yusef-Zadeh et al. 2010; Mills et al. 2011); and the prominent star-forming sites Sgr B2(N), Sgr B2(M), and Sgr B2(S) (e.g., Mehringer et al. 1993, 1995; de Pree et al. 1995, 1996; De Pree et al. 2015; Gaume et al. 1995).

The weaker continuum emission in the Dust Ridge and Sgr C tiles also morphologically agrees with previous detections, although for some sources we do not find observations in the literature at as high an angular resolution as ours. We compared with radio continuum images toward the Dust Ridge clouds (e.g., G0.253−0.025, Dust Ridge clouds c/e/f; Immer et al. 2012a; Rodríguez & Zapata 2013; Mills et al. 2015; Ludovici et al. 2016; Butterfield et al. 2018; Lu et al. 2019) and the Sgr C cloud (Forster & Caswell 2000; Lu et al. 2019), and found counterparts in our *C*-band continuum images.

Our observations recover emission at angular scales of ∼1″–60″ and are not sensitive to emission above the angular scale of 60″ (2.4 pc at the distance of the CMZ). Consequently, spatially extended structures such as diffuse H II regions, supernova remnants, and nonthermal filaments tend to be resolved out. This is evident toward the radio-bright zone around Sgr A* (∼3′ across; specifically, the Sgr A East supernova remnant shell; Zhao et al. 2016), as well as the radio filaments projected throughout the CMZ (usually a few arcminutes; Yusef-Zadeh et al. 2004; Lang et al. 2010), which are mostly resolved out in our observations.

3.2. Identification of Compact Continuum Sources

We identified compact sources from the *C*-band continuum emission, in which we search for UC H II regions later (see Section 4.1). The typical size of UC H II regions is $\lesssim$0.1 pc (Churchwell 2002), equivalent to $\lesssim$2.″5, and therefore, we should only consider compact (point-like) sources in our observations of ∼1″–2″ resolution. There are more extended (>2.″5) sources that correspond to known H II regions (e.g., in Sgr B2(M), Sgr B2(N), and Sgr A East; Gaume et al. 1995; Mills et al. 2011; De Pree et al. 2015), but we excluded them in the following discussion as they represent more evolved stages of star formation.

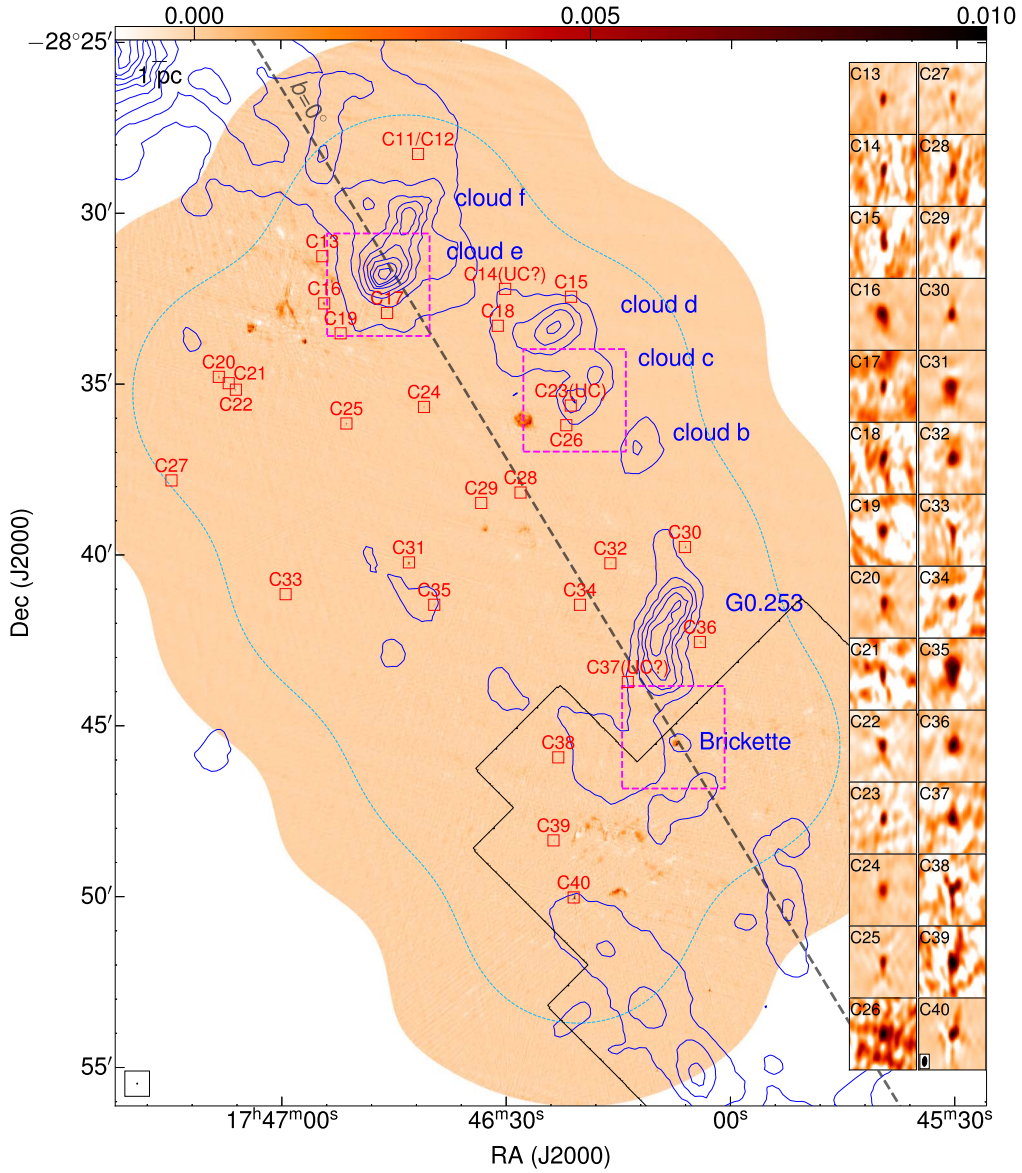

Figure 3. Overview of the Dust Ridge tile. Contours and symbols are the same as in Figure 2. The black contour shows the coverage of the *HST* Paschen-α survey of Wang et al. (2010; see Section 4.1.2).

As discussed in Section 2, the continuum images are dynamic range limited, especially in the Sgr A and Sgr B2 tiles, where the thermal noise level ($\sim$20 μJy beam^{-1}) cannot be achieved. In addition, partially resolved-out sources cannot be completely cleaned and therefore increase the local rms. As a result, the rms of the continuum images varies greatly across the maps. To account for this varying rms level, we first constructed a noise map for each tile with primary-beam-corrected images, using the SExtractor package (Bertin & Arnouts 1996). As recommended in Hales et al. (2012), we used a mesh size of 27 $\times$ 27 pixels, corresponding to $\sim$80 independent beams in one mesh given that one beam encompasses about 3 pixels in one dimension. The resulting noise map achieves a balance between reflecting local rms variations and having a statistically robust sample of independent measurements within each mesh. The median noise level within the FWHM is 229 μJy beam^{-1} for the Sgr B2 tile, 105 μJy beam^{-1} for the Dust Ridge tile, 170 μJy beam^{-1} for the Sgr A tile, and 53 μJy beam^{-1} for the Sgr C tile.

To identify compact sources, we employed the BLOBCAT software (Hales et al. 2012), which has been adopted in several radio continuum surveys (e.g., Bihr et al. 2016; Wang et al. 2018). BLOBCAT utilizes the flood-fill algorithm to detect and catalog blobs, or islands of pixels representing sources, in 2D images. The noise map and the primary-beam-corrected image for each tile were fed into BLOBCAT. We set the detection threshold to 5σ and the flooding threshold to 2.6σ as recommend in Hales et al. (2012). In addition, to search for compact sources, we put an upper limit of 800 pixels for the source area, which correspond to a radius of $\sim$0.2 pc. This upper limit is slightly relaxed compared with the usually adopted size of UC H II regions ($\lesssim$0.1 pc) to allow for some sources that appear spatially blended due to strong side lobes. The largest radius we actually found is 0.16 pc (for C56; see Table 3).

We further performed a visual inspection of the identified sources and rejected artifacts, including apparent side lobes,

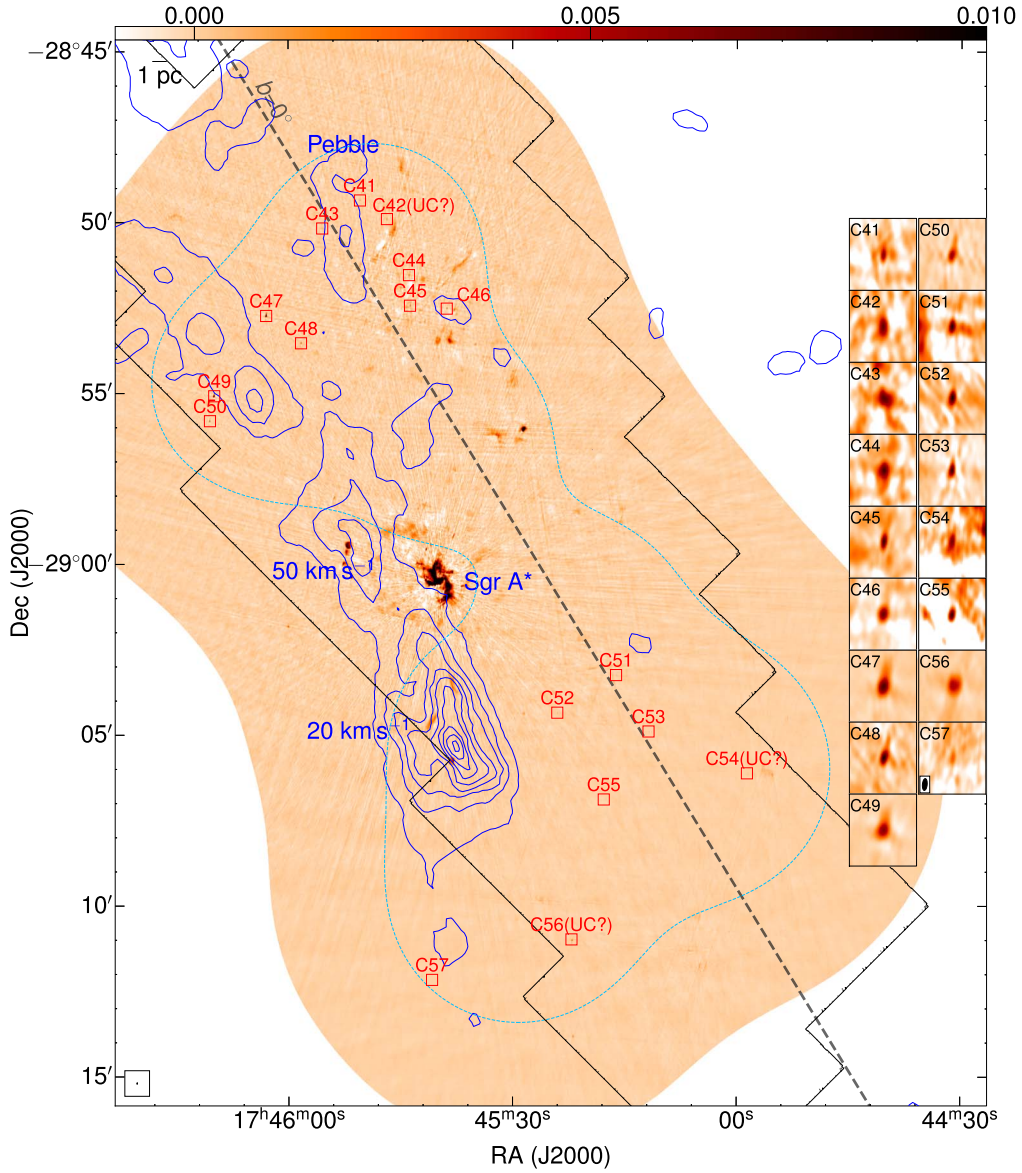

Figure 4. Overview of the Sgr A tile. Contours and symbols are the same as in Figure 2. The black contour shows the coverage of the *HST* Paschen-α survey of Wang et al. (2010; see Section 4.1.2). Note that the primary beam response of the mosaic, whose FWHM is represented by the green dashed loop, is unusually low around Sgr A*. This is because the visibility data of this field is downweighted for the imaging due to higher noise than other fields in the mosaic.

partially resolved-out extended sources, and irregularly shaped sources that are not point like. Sources outside of the FWHM of the primary beam response were also excluded. Nonetheless, toward extended structures that are significantly resolved out, residual emission may still be misclassified as compact sources. For example, C42 spatially overlaps with the Arched Filaments (Yusef-Zadeh et al. 1984; Lang et al. 2001) that are mostly resolved-out in our data and therefore could just be the residual.

Finally, we identified 104 compact sources. We took peak coordinates, peak intensities, and integrated fluxes from the output of BLOBCAT. We calculated areas of the sources using the number of pixels reported by BLOBCAT, subtracted the beam area quadratically (assuming a Gaussian beam with major and minor axes reported in Section 2), and obtained beam-deconvolved effective radii of the compact sources. Spectral indices and their uncertainties at the peak intensities, derived using the multiterm tclean of the *C*-band continuum in Section 2, were extracted from the data products. These properties are listed in Table 3. The positions of the compact sources are marked by red boxes in Figures 2–5, where some closely packed ones are marked by one single box.

Note that we avoided the Sgr B2 region (the dashed box in Figure 2), the UC (and hypercompact, HC) H II population of which has been studied with higher angular resolution and better sensitivity than ours as well as supplemental evidence from radio recombination lines (e.g., Gaume et al. 1995; de Pree et al. 1996; Sewilo et al. 2004; Zhao & Wright 2011; De Pree et al. 2015). A total of 41 UC/HC H II regions were previously identified in Sgr B2 (Gaume et al. 1995; De Pree et al. 2015).

Similarly, we avoided the Sgr A* region (the central brightest part in Figure 4), where our *C*-band continuum image is dynamic range limited and spatial filtering of the VLA causes significant artifacts. In addition, due to the high noise level in the visibility data, this region is significantly downweighted among the mosaicked pointings in Figure 4 and lies mostly

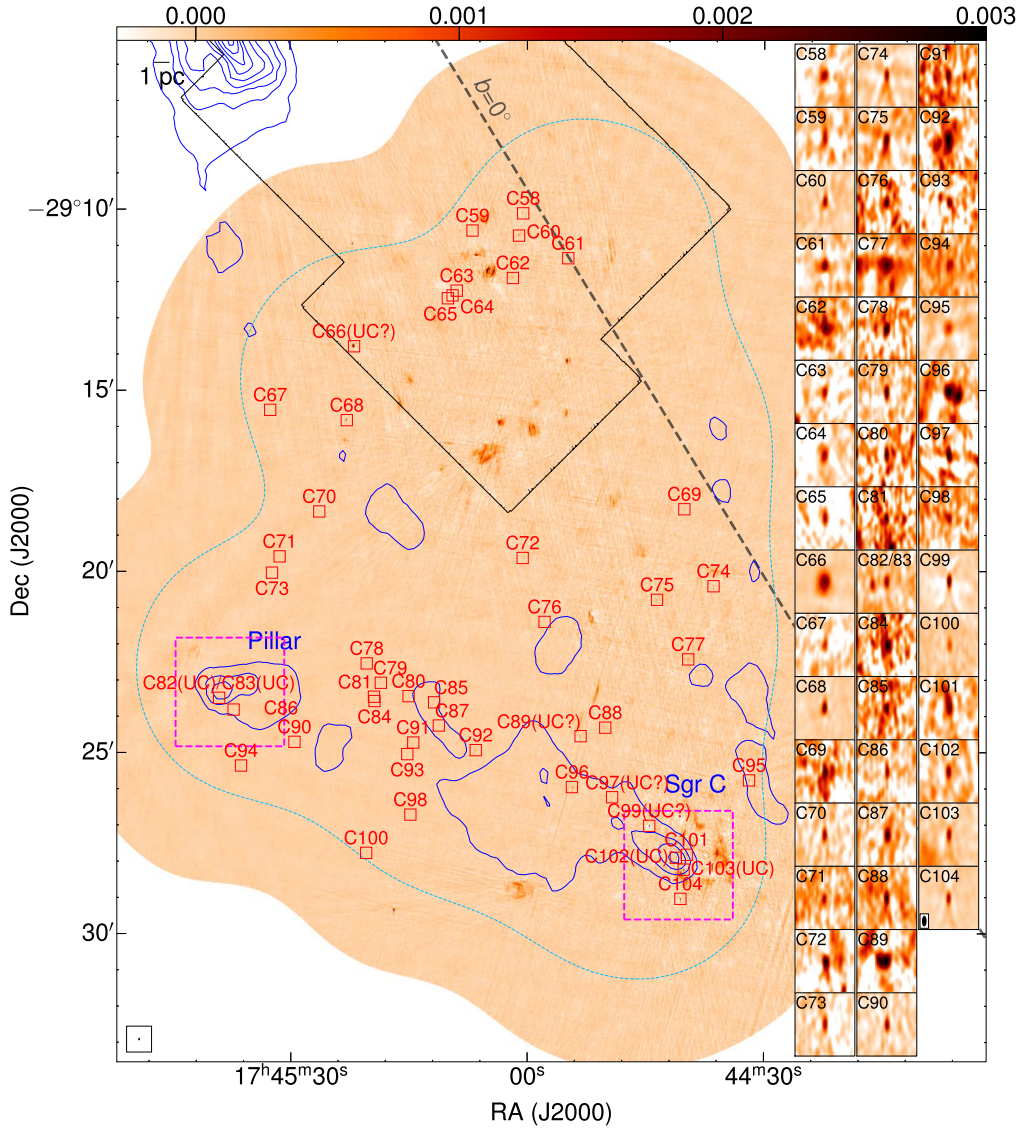

Figure 5. Overview of the Sgr C tile. Contours and symbols are the same as in Figure 2. The black contour shows the coverage of the *HST* Paschen-α survey of Wang et al. (2010; see Section 4.1.2).

outside of the FWHM of the primary beam response. Although we recover a few known compact structures (e.g., the four H II regions in Sgr A East, the compact radio source G−0.04−0.12; Mills et al. 2011), we do not discuss them further.

As shown in Figures 2–5, the identified continuum sources are not randomly distributed among the four tiles as well as within the tiles. For example, there is a concentration of sources, from C78 to C98, toward the lower-left region of the Sgr C tile in Figure 5. This is because we use the detection threshold of 5σ where the σ value is position dependent. In this case, more sources tend to be identified where the noise level is lower. If we use a fixed detection threshold of five times the median noise level of the Sgr B2 tile (the highest noise among the four tiles), the numbers of identified sources in the four tiles are 11, 12, 13, and 8, respectively, which are within the uncertainty of $\sim$3 around the mean value of 11 assuming Poisson statistics. Therefore, the nonuniformity among the tiles, if there is any, is not clear based on the current data. The lower-left region of the Sgr C tile has the lowest noise among all the images ($\sim$30 μJy beam^{-1}); therefore, we were able to identify a large number of sources.

Assuming the continuum emission is solely contributed by optically thin free–free emission from UC H II regions, we estimated the detection limit in terms of stellar masses powering the UC H II regions. With a characteristic election temperature of 8000 K and following Mezger et al. (1974), we calculated ionizing photon rates corresponding to the 5σ detection threshold, in which we used the median rms level in each tile as the 1σ level. Then, by comparing with the expected ionizing photon rates of ZAMS stars (e.g., Davies et al. 2011), we obtained the detection limit of the continuum emission, which ranges from 10.1 $M_\odot$ in the Sgr C tile (where the median noise level is the lowest) to 11.6 $M_\odot$ in the Sgr B2 tile (where the median noise level is the highest). Around Sgr A* and Sgr B2, where the rms is higher than 320 μJy beam^{-1}, the 5σ detection limit is $\gtrsim$12 $M_\odot$, though such regions are a small fraction of the coverage area (<9%), and we have avoided these two regions in our identification. Therefore, except for small regions around bright continuum sources in the Sgr B2 and Sgr A tiles, the continuum observation is complete to free–free emission from all stars above 10–11 $M_\odot$ (B1 type and earlier) in 91% of the covered area.

Table 3
Properties of Compact Sources in *C*-band Continuum

ID	R.A. and Decl. (J2000)	$r_{\rm eff}$[a] (pc)	$I_{\rm peak}$[b] (mJy beam^{-1})	$F_{\rm int}$[b] (mJy)	$\alpha \pm \sigma(\alpha)$[b,c]	*HST* Pa-α (Ref: W10)	*WISE* H II Regions (Ref: A14)	*Spitzer* YSOs (Refs: Y09, A11)	*Herschel* $N(H_2)$ (Ref: B11)	Counterparts[d] Against UC H II	Previous Detections[e] of Compact Continuum Sources	Remarks
C1	17:46:53.82, −28:19:00.38	0.01	0.99 ± 0.19	1.19 ± 0.19	−2.67 ± 0.26	⋯	G000.674 +00.083		N	X(M06)		
C2	17:47:40.33, −28:20:06.11	0.03	2.95 ± 0.23	3.25 ± 0.23	−0.14 ± 0.01	⋯			Y			UC?
C3	17:47:43.10, −28:20:30.38	0.02	1.99 ± 0.19	1.69 ± 0.17	−0.24 ± 0.01	⋯			Y			
C4	17:47:22.61, −28:24:54.22	UR	2.70 ± 0.54	3.11 ± 0.54	−2.71 ± 1.81	⋯			Y			
C5	17:47:23.36, −28:25:33.81	0.02	3.23 ± 0.58	4.57 ± 0.60	−1.61 ± 0.94	⋯			Y	X(M06, M09)		
C6	17:46:38.51, −28:25:34.95	0.06	7.98 ± 0.46	12.09 ± 0.63	−0.48 ± 0.01	⋯			N			
C7	17:46:37.94, −28:25:51.14	0.03	2.60 ± 0.25	2.98 ± 0.26	0.82 ± 0.03	⋯			N			
C8	17:46:37.57, −28:26:00.44	0.03	2.71 ± 0.28	3.20 ± 0.28	−0.52 ± 0.02	⋯			N			
C9	17:46:55.61, −28:26:07.60	0.04	1.35 ± 0.19	3.56 ± 0.25	0.43 ± 0.02	⋯			Y			UC?
C10	17:47:27.09, −28:27:24.80	0.03	1.45 ± 0.26	3.62 ± 0.30	−2.32 ± 1.86	⋯		SSTGC805200	Y			UC?
C11	17:46:41.77, −28:28:16.71	0.02	3.53 ± 0.30	3.19 ± 0.29	−1.10 ± 0.03	⋯			Y		2LC000.520 +0.040(L08)	
C12	17:46:41.86, −28:28:18.21	0.02	2.14 ± 0.27	2.10 ± 0.26	−3.50 ± 0.63	⋯			Y			
C13	17:46:54.52, −28:31:16.21	0.04	3.87 ± 0.27	3.79 ± 0.25	0.00 ± 0.01	⋯			N			
C14	17:46:30.17, −28:32:13.62	0.02	0.42 ± 0.06	0.45 ± 0.06	−0.70 ± 0.57	⋯			Y			UC?
C15	17:46:21.38, −28:32:27.39	0.04	0.45 ± 0.07	0.85 ± 0.08	−1.60 ± 0.98	⋯			Y		2LC000.422 +0.068(L08)	
C16	17:46:54.28, −28:32:39.01	0.13	6.96 ± 0.41	25.60 ± 1.29	−0.04 ± 0.01	⋯			N		2LC000.481 −0.037(L08)	
C17	17:46:45.90, −28:32:55.88	0.03	0.99 ± 0.12	0.97 ± 0.12	−1.69 ± 0.59	⋯			Y			
C18	17:46:31.14, −28:33:18.42	0.03	0.43 ± 0.07	0.74 ± 0.08	−2.52 ± 1.87	⋯			Y			
C19	17:46:52.09, −28:33:31.53	0.03	0.72 ± 0.13	1.15 ± 0.13	−0.24 ± 0.11	⋯			N			
C20	17:47:08.34, −28:34:47.82	0.10	6.77 ± 0.41	15.14 ± 0.78	−0.80 ± 0.05	⋯			N		2LC000.477-0.100(L08)	
C21	17:47:07.02, −28:34:58.94	0.02	0.86 ± 0.15	1.16 ± 0.16	−1.72 ± 0.70	⋯			N			
C22	17:47:06.06, −28:35:10.36	0.07	4.14 ± 0.27	6.48 ± 0.36	−1.24 ± 0.11	⋯			N			
C23		0.03	0.90 ± 0.07	0.83 ± 0.07	−0.22 ± 0.10	⋯			Y			UC

Table 3
(Continued)

ID	R.A. and Decl. (J2000)	$r_{\rm eff}$[a] (pc)	$I_{\rm peak}$[b] (mJy beam^{-1})	$F_{\rm int}$[b] (mJy)	$\alpha \pm \sigma(\alpha)$[b,c]	*HST* Pa-α (Ref: W10)	*WISE* H II Regions (Ref: A14)	*Spitzer* YSOs (Refs: Y09, A11)	*Herschel* $N(H_2)$ (Ref: B11)	Counterparts[d] Against UC H II	Previous Detections[e] of Compact Continuum Sources	Remarks
	17:46:21.42, −28:35:38.49							SSTGC639320, EGO g16				
C24	17:46:40.98, −28:35:40.90	0.08	3.18 ± 0.21	6.77 ± 0.36	−2.27 ± 0.23	⋯			N		2LC000.413-0.022(L08)	
C25	17:46:51.33, −28:36:09.94	0.09	7.06 ± 0.40	10.61 ± 0.55	−2.32 ± 0.11	⋯			N	X(M06)	2LC000.426-0.058(L08)	
C26	17:46:22.01, −28:36:13.00	0.06	0.32 ± 0.06	1.29 ± 0.09	−1.81 ± 0.97	⋯			N			
C27	17:47:14.67, −28:37:49.51	0.03	2.05 ± 0.19	2.16 ± 0.19	−2.10 ± 0.39	⋯			N			
C28	17:46:28.11, −28:38:11.22	0.03	0.64 ± 0.11	1.07 ± 0.12	−3.41 ± 1.70	⋯			N			
C29	17:46:33.35, −28:38:29.52	0.04	0.98 ± 0.14	1.52 ± 0.15	−4.31 ± 1.50	⋯			N			
C30	17:46:06.18, −28:39:46.76	0.10	8.03 ± 0.45	12.89 ± 0.66	0.13 ± 0.01	⋯			N		C(I12), JVLA2(R13)	
C31	17:46:43.00, −28:40:13.89	0.12	7.45 ± 0.45	30.84 ± 1.55	−0.95 ± 0.04	⋯			N		2LC000.352-0.068(L08)	
C32	17:46:16.12, −28:40:15.36	0.09	1.50 ± 0.12	4.07 ± 0.22	−0.56 ± 0.13	⋯			N		JVLA7(R13)	
C33	17:46:59.46, −28:41:09.55	0.04	0.85 ± 0.09	1.29 ± 0.10	−0.93 ± 0.44	⋯			N			
C34	17:46:20.18, −28:41:28.29	0.02	0.59 ± 0.11	0.76 ± 0.11	−2.87 ± 1.72	⋯			N			
C35	17:46:39.62, −28:41:28.31	0.12	1.04 ± 0.09	7.15 ± 0.37	−1.50 ± 0.34	⋯			Y			
C36	17:46:04.17, −28:42:33.54	0.09	3.06 ± 0.20	8.32 ± 0.43	0.12 ± 0.02	⋯			N		B(I12), JVLA1(R13)	
C37	17:46:13.79, −28:43:43.84	0.05	0.81 ± 0.11	1.88 ± 0.14	−0.41 ± 0.17	⋯		SSTGC618018?	Y		JVLA6(R13)	UC?
C38	17:46:23.07, −28:45:56.20	0.06	0.99 ± 0.13	2.76 ± 0.18	−3.01 ± 1.01	N			N			
C39	17:46:23.70, −28:48:22.00	0.05	0.79 ± 0.13	2.57 ± 0.18	−2.33 ± 0.73	Y			N			
C40	17:46:21.00, −28:50:02.19	0.11	27.38 ± 1.51	64.18 ± 3.22	0.77 ± 0.01	N			Y		N3(Y87)	
C41	17:45:50.43, −28:49:21.66	0.04	2.05 ± 0.25	2.41 ± 0.26	2.18 ± 0.96	Y			N	WR*(L05), X(M06,M09)	AR1(L05)	
C42	17:45:46.82, −28:49:54.38	0.06	2.18 ± 0.36	5.76 ± 0.44	0.31 ± 0.12	Y			N			UC?
C43	17:45:55.48, −28:50:10.81	0.07	1.22 ± 0.20	4.63 ± 0.30	0.16 ± 0.08	Y			N	Mi*(G01)		
C44	17:45:43.88, −28:51:32.79	0.08	2.71 ± 0.32	7.46 ± 0.47	0.29 ± 0.08	Y			N	F*?(H19)	H13(L01)	
C45		0.08	4.94 ± 0.43	7.76 ± 0.51	−0.41 ± 0.08	Y			N	F*?(H19)	H12(L01)	

Table 3
(Continued)

ID	R.A. and Decl. (J2000)	$r_{\rm eff}$[a] (pc)	$I_{\rm peak}$[b] (mJy beam^{-1})	$F_{\rm int}$[b] (mJy)	$\alpha \pm \sigma(\alpha)$[b,c]	*HST* Pa-α (Ref: W10)	*WISE* H II Regions (Ref: A14)	*Spitzer* YSOs (Refs: Y09, A11)	*Herschel* $N(H_2)$ (Ref: B11)	Counterparts[d] Against UC H II	Previous Detections[e] of Compact Continuum Sources	Remarks
	17:45:43.75, −28:52:26.50											
C46	17:45:38.83, −28:52:31.61	0.05	3.55 ± 0.33	5.39 ± 0.38	−0.39 ± 0.09	Y			Y	F*?(H19)	H11(L01)	
C47	17:46:02.98, −28:52:44.33	0.14	16.57 ± 0.93	48.27 ± 2.43	−0.29 ± 0.01	Y			N	PN(P16)	N1(Y87), 2LC000.098-0.051(L08)	
C48	17:45:58.32, −28:53:32.39	0.07	4.03 ± 0.29	6.05 ± 0.35	0.31 ± 0.07	N			N	X(Z18)		
C49	17:46:09.93, −28:55:05.23	0.12	14.98 ± 0.87	39.66 ± 2.01	−0.39 ± 0.02	N			N		2LC000.078-0.093(L08)	
C50	17:46:10.51, −28:55:49.02	0.07	7.21 ± 0.46	9.99 ± 0.56	0.72 ± 0.09	N			N			
C51	17:45:16.17, −29:03:15.04	0.02	1.10 ± 0.16	1.09 ± 0.16	1.25 ± 1.03	Y			N	WR*(M10), X(M09,Z18)		
C52	17:45:24.04, −29:04:21.09	0.05	1.41 ± 0.13	1.62 ± 0.13	−0.93 ± 0.60	N			N			
C53	17:45:11.82, −29:04:53.99	0.04	1.44 ± 0.11	1.24 ± 0.10	−0.53 ± 0.35	N			N			
C54	17:44:58.63, −29:06:07.32	0.04	0.39 ± 0.08	0.78 ± 0.08	−0.32 ± 0.19	Y			N			UC?
C55	17:45:17.81, −29:06:53.45	UR	0.42 ± 0.06	0.32 ± 0.06	−4.12 ± 3.31	N			N	X(M09)		
C56	17:45:22.12, −29:10:59.18	0.16	4.04 ± 0.24	15.28 ± 0.77	−0.71 ± 0.13	Y		SSTGC476516	N			UC?
C57	17:45:40.82, −29:12:10.31	UR	0.54 ± 0.10	0.50 ± 0.10	−2.19 ± 0.58	···			N			
C58	17:45:00.55, −29:10:07.70	0.04	0.58 ± 0.08	1.15 ± 0.10	−1.86 ± 0.58	N			N			
C59	17:45:06.96, −29:10:36.21	0.04	0.66 ± 0.13	1.69 ± 0.15	−2.35 ± 0.70	Y			N			
C60	17:45:01.08, −29:10:44.60	0.06	2.49 ± 0.16	3.08 ± 0.18	0.11 ± 0.01	N			N	X(M06,M09)		
C61	17:44:54.84, −29:11:22.07	0.05	0.52 ± 0.06	0.85 ± 0.07	−0.32 ± 0.13	N			N			
C62	17:45:01.85, −29:11:54.80	0.07	0.35 ± 0.07	2.04 ± 0.12	−0.65 ± 0.26	N			N			
C63	17:45:08.96, −29:12:15.81	0.02	0.53 ± 0.10	0.68 ± 0.10	−0.46 ± 0.19	Y		SSTGC441299	N	X(06)		
C64	17:45:09.48, −29:12:23.61	0.05	0.79 ± 0.10	1.61 ± 0.12	−1.95 ± 0.51	Y			N			
C65	17:45:10.08, −29:12:28.41	0.02	0.49 ± 0.10	0.63 ± 0.10	−1.49 ± 0.67	Y			N			
C66	17:45:21.95, −29:13:47.88	0.14	4.36 ± 0.24	19.92 ± 1.00	0.40 ± 0.01	Y			N		2LC359.720-0.106(L08)	UC?

Table 3
(Continued)

ID	R.A. and Decl. (J2000)	$r_{\rm eff}$[a] (pc)	$I_{\rm peak}$[b] (mJy beam^{-1})	$F_{\rm int}$[b] (mJy)	$\alpha \pm \sigma(\alpha)$[b,c]	*HST* Pa-α (Ref: W10)	*WISE* H II Regions (Ref: A14)	*Spitzer* YSOs (Refs: Y09, A11)	*Herschel* $N(H_2)$ (Ref: B11)	Counterparts[d] Against UC H II	Previous Detections[e] of Compact Continuum Sources	Remarks
C67	17:45:32.57, −29:15:33.08	0.01	0.42 ± 0.08	0.48 ± 0.08	−1.90 ± 0.70	···			N			
C68	17:45:22.87, −29:15:50.27	0.07	2.52 ± 0.14	2.94 ± 0.15	0.41 ± 0.04	···			N			
C69	17:44:40.13, −29:18:17.72	0.04	0.20 ± 0.04	0.47 ± 0.04	−2.05 ± 1.34	···			N			
C70	17:45:26.36, −29:18:21.44	0.03	0.47 ± 0.05	0.48 ± 0.05	−0.60 ± 0.31	···			N			
C71	17:45:31.39, −29:19:35.80	0.02	0.25 ± 0.05	0.34 ± 0.05	−2.10 ± 1.02	···			N			
C72	17:45:00.61, −29:19:38.60	0.04	0.33 ± 0.05	0.66 ± 0.06	−2.99 ± 1.75	···		SSTGC419271	N			
C73	17:45:32.36, −29:20:02.79	0.04	0.50 ± 0.05	0.65 ± 0.06	−3.14 ± 1.30	···			N			
C74	17:44:36.42, −29:20:25.17	0.08	1.54 ± 0.12	2.67 ± 0.16	−2.34 ± 0.33	···	G359.541 −00.023		N		2LC359.540-0.023(L08)	
C75	17:44:43.58, −29:20:47.77	0.06	0.59 ± 0.07	1.41 ± 0.09	−1.62 ± 0.61	···		SSTGC374813	N			
C76	17:44:57.83, −29:21:24.49	0.01	0.16 ± 0.03	0.20 ± 0.03	−2.06 ± 1.71	···			N			
C77	17:44:39.63, −29:22:26.42	0.08	0.51 ± 0.10	3.54 ± 0.20	−2.42 ± 0.60	···			N			
C78	17:45:20.36, −29:22:33.18	0.04	0.16 ± 0.03	0.36 ± 0.03	−2.03 ± 1.61	···			N			
C79	17:45:18.57, −29:23:05.29	0.03	0.29 ± 0.03	0.33 ± 0.03	−2.35 ± 1.64	···			N			
C80	17:45:15.06, −29:23:27.51	0.01	0.14 ± 0.03	0.16 ± 0.03	−0.43 ± 0.38	···			N			
C81	17:45:19.45, −29:23:28.39	UR	0.13 ± 0.03	0.13 ± 0.03	−2.51 ± 1.90	···			N			
C82	17:45:39.07, −29:23:30.00	0.04	0.46 ± 0.05	0.60 ± 0.05	−0.67 ± 0.31	···		EGO g26	Y			UC
C83	17:45:39.35, −29:23:30.90	0.03	0.39 ± 0.05	0.48 ± 0.05	−1.89 ± 0.98	···		EGO g26	Y			UC
C84	17:45:19.38, −29:23:35.59	0.05	0.13 ± 0.03	0.47 ± 0.03	−2.35 ± 1.79	···			N			
C85	17:45:11.83, −29:23:37.71	0.02	0.16 ± 0.03	0.21 ± 0.03	−1.72 ± 1.38	···			Y			
C86	17:45:37.24, −29:23:49.53	0.02	0.27 ± 0.04	0.30 ± 0.04	0.17 ± 0.11	···			Y	X(M06)		
C87	17:45:11.23, −29:24:16.11	0.05	0.29 ± 0.04	0.57 ± 0.04	−3.27 ± 2.27	···			Y			
C88	17:44:50.13, −29:24:19.63	0.05	0.44 ± 0.05	0.70 ± 0.06	−1.99 ± 1.05	···			N			
C89		0.08	0.37 ± 0.05	1.68 ± 0.09	−2.85 ± 1.15	···		SSTGC400062	N			UC?

Table 3
(Continued)

ID	R.A. and Decl. (J2000)	$r_{\rm eff}$[a] (pc)	$I_{\rm peak}$[b] (mJy beam^{-1})	$F_{\rm int}$[b] (mJy)	$\alpha \pm \sigma(\alpha)$[b,c]	*HST* Pa-α (Ref: W10)	*WISE* H II Regions (Ref: A14)	*Spitzer* YSOs (Refs: Y09, A11)	*Herschel* $N(H_2)$ (Ref: B11)	Counterparts[d] Against UC H II	Previous Detections[e] of Compact Continuum Sources	Remarks
	17:44:53.25, −29:24:33.76						G359.513 −00.111					
C90	17:45:29.53, −29:24:43.02	0.04	0.69 ± 0.05	0.68 ± 0.05	−1.41 ± 0.44	⋯			N			
C91	17:45:14.47, −29:24:44.31	0.02	0.15 ± 0.03	0.24 ± 0.03	−4.05 ± 2.48	⋯			N			
C92	17:45:06.55, −29:24:56.91	0.08	0.20 ± 0.03	1.07 ± 0.06	−1.84 ± 1.19	⋯			N			
C93	17:45:15.22, −29:25:03.51	0.00	0.15 ± 0.03	0.17 ± 0.03	−2.02 ± 1.39	⋯			N			
C94	17:45:36.30, −29:25:22.24	0.06	0.30 ± 0.05	1.21 ± 0.08	−4.07 ± 1.18	⋯			N			
C95	17:44:31.89, −29:25:46.70	0.05	1.43 ± 0.17	2.96 ± 0.21	−2.01 ± 0.28	⋯			Y		2LC359.456-0.055(L08)	
C96	17:44:54.35, −29:25:58.07	0.10	0.37 ± 0.05	2.31 ± 0.12	−2.14 ± 0.91	⋯			Y			
C97	17:44:49.25, −29:26:14.83	0.03	0.25 ± 0.05	0.41 ± 0.05	−1.46 ± 1.17	⋯		SSTGC390425	Y			UC?
C98	17:45:14.84, −29:26:43.71	0.03	0.23 ± 0.05	0.39 ± 0.05	−1.90 ± 1.01	⋯			N			
C99	17:44:44.54, −29:27:02.18	0.04	3.74 ± 0.22	3.35 ± 0.19	0.69 ± 0.04	⋯			Y			UC?
C100	17:45:20.44, −29:27:46.98	0.04	1.05 ± 0.10	1.34 ± 0.10	−2.54 ± 0.59	⋯			N			
C101	17:44:39.78, −29:27:50.12	0.07	0.97 ± 0.17	4.88 ± 0.29	−1.69 ± 0.23	⋯			Y			
C102	17:44:41.16, −29:27:54.94	0.03	1.08 ± 0.14	1.41 ± 0.15	−0.35 ± 0.07	⋯			Y		H1(L19)	UC
C103	17:44:40.17, −29:28:14.72	0.07	4.37 ± 0.30	6.16 ± 0.36	−0.53 ± 0.03	⋯		EGO g29	Y		359.44−0.10A (F00), H3(L19)	UC
C104	17:44:40.58, −29:29:03.03	0.07	6.31 ± 0.37	7.03 ± 0.38	−0.63 ± 0.02	⋯			Y		359.44−0.10B (F00), 2LC359.425-0.111(L08)	

Notes.
[a] Unresolved sources are marked by "UR."
[b] Intensities, fluxes, and spectral indices have been corrected for primary-beam response.
[c] The systematic uncertainty in spectral indices of 0.05 is not listed.
[d] Counterparts that would argue against UC H II regions, with references in parentheses. The object types generally follow the abbreviation convention of SIMBAD: X—X-ray sources; Mi*—Mira variable stars; F*?—possible field stars; WR*—Wolf–Rayet stars; PN—planetary nebula.
[e] Identifiers of previous detections of compact radio continuum emission using radio interferometers, with references in parentheses.

References. A11: An et al. (2011). A14: Anderson et al. (2014). B11: Battersby et al. (2011). F00: Forster & Caswell (2000). G01: Glass et al. (2001). H19: Hankins et al. (2019). I12: Immer et al. (2012a). L01: Lang et al. (2001). L05: Lang et al. (2005). L08: Lazio & Cordes (2008). L19: Lu et al. (2019). M10: Mauerhan et al. (2010b). M06: Muno et al. (2006). M09: Muno et al. (2009). P16: Parker et al. (2016). R13: Rodríguez & Zapata (2013). W10: Wang et al. (2010). Y87: Yusef-Zadeh & Morris (1987a). Y09: Yusef-Zadeh et al. (2009). Z18: Zhu et al. (2018).

Several compact sources have been reported in previous radio interferometer observations (not necessarily using the same frequency band as ours; e.g., Yusef-Zadeh & Morris 1987a; Forster & Caswell 2000; Lang et al. 2001; Lazio & Cordes 2008; Immer et al. 2012a; Rodríguez & Zapata 2013; Lu et al. 2019). We listed corresponding references and identifiers in Table 3. In total, 24 out of the 104 compact sources have been identified before, and the remaining 80 compact sources are likely new detections. Among these previous observations, Lazio & Cordes (2008) conducted a high-angular-resolution ($\sim 2''$), high-sensitivity (thermal noise level $\sim 50\,\mu$Jy beam^{-1}, although the measured noise level can be 10 times higher) survey of compact radio sources at 1.4 GHz, covering a larger area than ours. Sixty of their identified compact sources fall within our observation coverage, and 13 have counterparts in our catalog (see the 2LC objects in Table 3). Excluding 18 sources that are found in the Sgr B2 and Sgr A* regions we have avoided, there are 29 sources that are not included in our catalog. We compared these sources with our data and noted that most of them are diffuse in our images, and therefore were not identified as compact sources by us. This accounts for 22 of the Lazio & Cordes (2008) sources not in our catalog. The other seven sources not in our catalog all present steep spectra with spectral indices of $\lesssim -2$ (Table 8 of Lazio & Cordes 2008), and therefore are too weak at the *C*-band and probably missed by our observations.

3.3. CH_3OH Masers

We manually identified 6.668 GHz CH_3OH masers in the images. After self-calibration, the dynamic range was significantly improved, and the images were able to achieve the thermal noise level (~ 8 mJy beam$^{-1} \in 0.35$ km s^{-1}) except for a few channels in the Sgr B2 tile. Therefore, identification of masers is straightforward with a visual inspection of maximum intensity maps (the eighth moment maps as defined in CASA). We defined the detection level for maser sources to be above the 5σ rms noise level and be found in at least two channels, where 1σ equals 8 mJy beam^{-1}per 0.35 km s^{-1} channel. The corresponding brightness temperature criterion is above 10^3 K. Therefore, any identified emission should be nonthermal, and as such should be masers, given typical gas temperatures of $\lesssim 300$ K in the CMZ (Ao et al. 2013; Ginsburg et al. 2016; Krieger et al. 2017; Lu et al. 2017). Multiple velocity components along the same line of sight were classified as a single maser. In the end, we identified 23 masers. Their positions are marked in Figure 6, spectra shown in Figure 7, and properties listed in Table 4.

All masers are spatially associated with molecular clouds in the CMZ or in the foreground. Fourteen masers are detected toward Sgr B2. Eleven of them have been reported in Houghton & Whiteoak (1995) and Caswell (1996), and three (M2, M3, and M9) are new detections. Three masers are detected in the Dust Ridge clouds: M15 is detected toward the Dust Ridge cloud e, which has been reported in Caswell (2009); M16 is detected toward Dust Ridge cloud c, which has been reported in Caswell (1996); and M17 is spatially adjacent to an H II region ("Brickette"; previous identified by, e.g., Giveon et al. 2005; Immer et al. 2012a; Rodríguez & Zapata 2013), which is also known (Caswell 1996). Three masers are detected toward Sgr C, among which two (M22, M23) have been reported in Caswell (1996) and one (M21) is a new detection. Finally, three masers are detected toward a cloud in field 27 ("Pillar"), which has been suggested to be in the foreground: the *Gaia* satellite measured a parallax of 1.3461 mas toward a bright source spatially coincident with the maser M20 (Gaia Collaboration et al. 2018), which translates to a distance of ~ 740 pc. Among the three masers detected in this cloud, M20 is known (Caswell 1996) and two (M18, M19) are new detections. In summary, 17 masers have been reported in the literature and six are new detections. We will discuss the implication for star formation in CMZ molecular clouds in Section 4.2.

Note that toward several positions in Sgr B2, the 6.668 GHz CH_3OH line also shows absorption (e.g., M3 and M5, Figure 7), but it is of much smaller magnitude compared with the maser emission, and therefore does not affect our identification of CH_3OH masers.

3.4. H_2CO Masers

H_2CO emission above the 5σ level is only detected toward Sgr B2, Dust Ridge cloud c, and Sgr C. Therefore, we manually identify H_2CO masers in the images of just these three regions. In Dust Ridge cloud c and Sgr C, H_2CO is only detected in emission, thus the identification of masers is straightforward. However, in Sgr B2, there is significant absorption which could substantially reduce the peak intensity of the maser emission.

With this consideration in mind, we checked the H_2CO image of Sgr B2 channel by channel and identified point sources above the 5σ level as compared to the surrounding continuum level (which could be negative, if affected by absorption) and detected in at least two channels. We found five H_2CO maser candidates, as shown in Figures 6 and 7, and three of them are indeed spatially coincident with strong H_2CO absorption (F1, F2, and F5 in Figure 7). All five H_2CO masers have been reported in Mehringer et al. (1994). Note that F2 shows a complex spectrum with strong emission and absorption features, among which we identified the channels at ~ 50 km s^{-1} as maser emission, in line with the finding of Mehringer et al. (1994).

As for Dust Ridge cloud c and Sgr C, we identified three H_2CO masers, as shown in Figures 6 and 7. The one in Dust Ridge cloud c has been reported in Ginsburg et al. (2015). The two H_2CO masers in Sgr C are new detections. Properties of the H_2CO masers are listed in Table 5.

4. Discussion

4.1. Identification of UC H II Regions

Five of the identified compact sources are spatially associated with class II CH_3OH masers (C23, C82, C83, C102, and C103; see Sections 3.3, 3.4, Figure 6) and are deemed to be UC H II regions. For the other compact sources, we attempt to investigate their nature by using *C*-band spectral indices and correlations with the hydrogen recombination line emission, infrared emission, high column densities, star clusters and massive field stars, evolved stars, and X-ray sources.

4.1.1. C-band Spectral Indices

Thermal free–free emission from UC H II regions usually present $\alpha = -0.1$ at $\lesssim 10$ GHz, while it could become optically thick in HC H II regions and present a higher spectral α of up to 2 (Sánchez-Monge et al. 2013). As shown in Table 3, after taking into account the fitting uncertainties and the systematic uncertainty (0.05), 25 out of the 104 sources present spectral indices between -0.1 and 2.

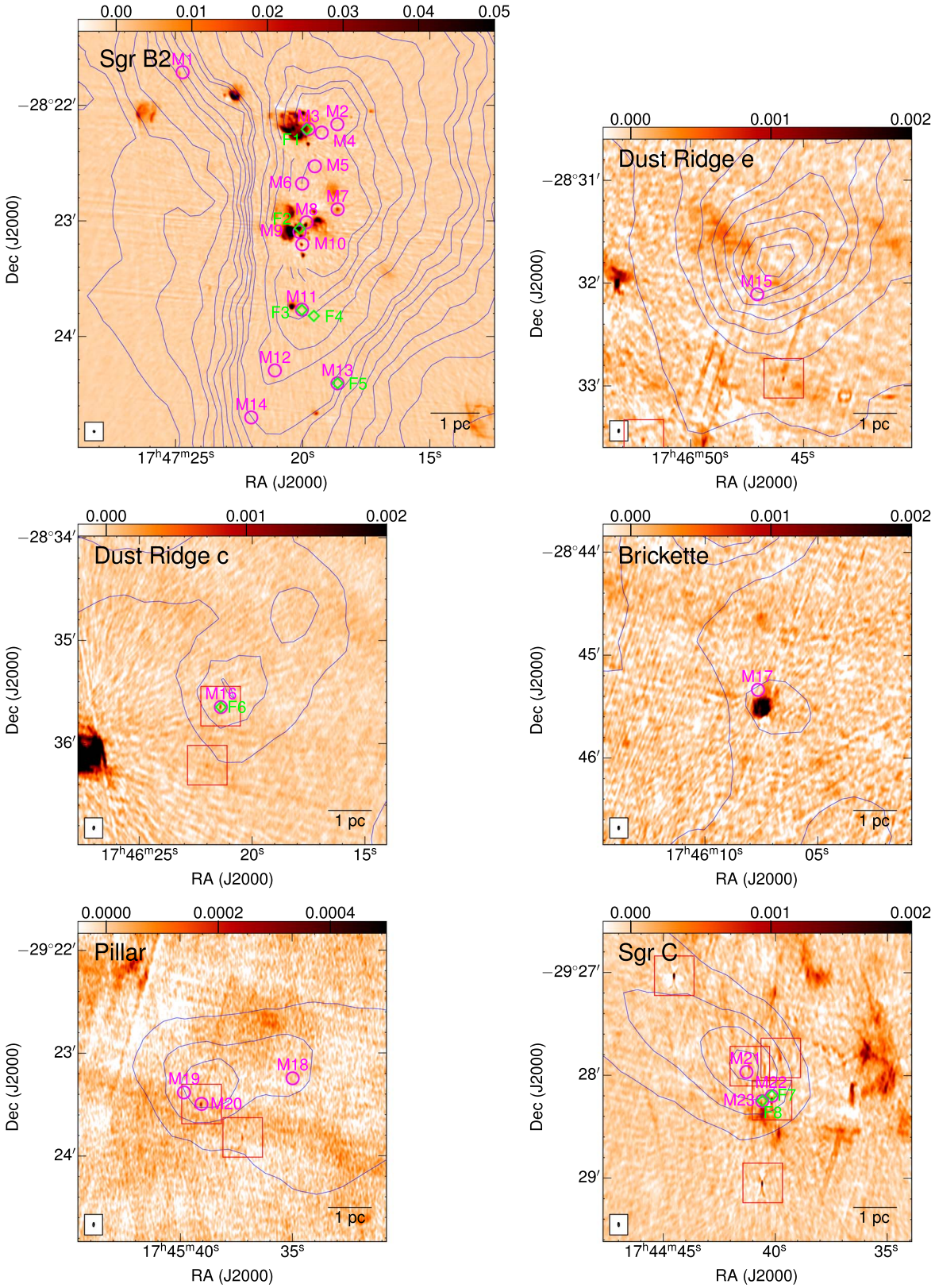

Figure 6. CH_3OH and H_2CO masers, marked by magenta circles and green diamonds, respectively. Background images show the VLA *C*-band continuum emission. Red boxes mark the compact sources that are identified in the continuum (see Figures 2–5).

However, there are several caveats in interpreting the derived spectral indices, which prevent us from confirming the nature of the compact sources.

The in-band spectral indices derived from our *C*-band data may be biased, and those derived with a wider frequency range may be different. For example, several known UC H II regions

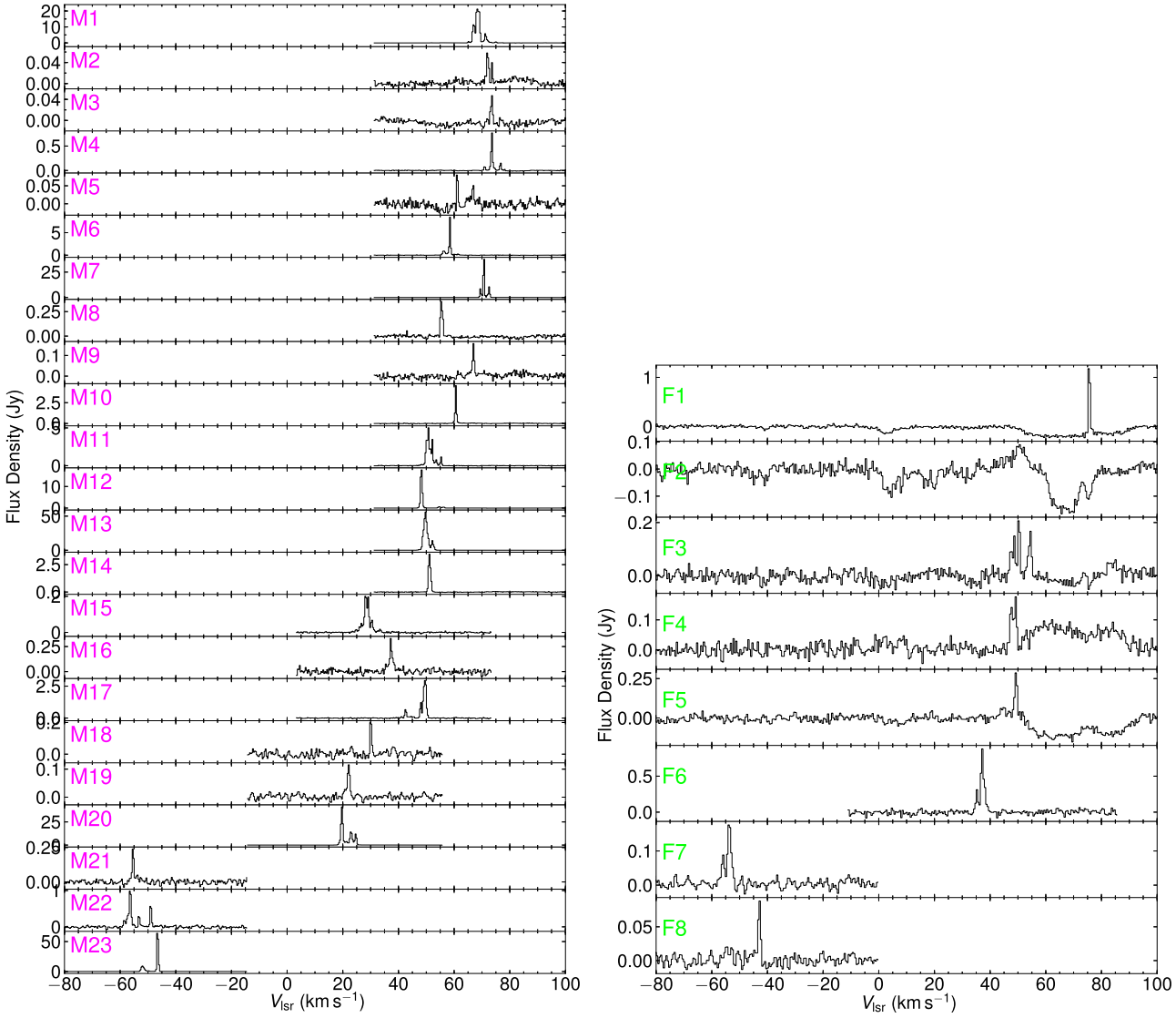

Figure 7. Spectra of the CH_3OH and H_2CO masers.

present spectral indices of <-0.1 in our data even after taking the uncertainties into account: C102 and C103 are embedded in the Sgr C cloud and have been identified as UC H II regions using *K*-band continuum at 23 GHz (labeled as H1 and H3 in Sgr C; Lu et al. 2019). Both of them are associated with class II CH_3OH masers, and C103 is also associated with a H_2CO maser (Sections 3.3, 3.4). Their *C*-band spectral indices are -0.35 and -0.53, respectively. However, if we estimate multiband spectral indices using the *C*-band and *K*-band data (assuming 5% and 10% flux uncertainties, respectively), the results are 0.34 ± 0.08 and -0.15 ± 0.08, respectively, and are consistent with thermal free–free emission from UC/HC H II regions. The other case is the source C40 (also known as N3; Yusef-Zadeh & Morris 1987a), which has a spectral index of 0.77 ± 0.01 in our measurement. However, it has been observed in multiple bands with the VLA (Ludovici et al. 2016), and a broken power-law spectral profile is found—at low frequencies (2–6 GHz), its spectral index is 0.56 ± 0.13, which is in agreement with our result within the uncertainties, but at high frequencies (10–36 GHz), the spectral index is -0.86 ± 0.11. As a result, it was ruled out to be a H II region by Ludovici et al. (2016) and could be a background AGN as suggested by N. Butterfield et al. (2019, in preparation).

Therefore, the *C*-band spectral indices alone are insufficient to confirm the nature of the sources. In the next section, we try to correlate the compact sources with Pa-α emission, infrared surveys, high column densities, and X-ray observations to more robustly search for UC H II region candidates.

4.1.2. Correlation with Other Surveys that Argue for UC H II Regions

First, we compare the identified compact sources with the *Hubble Space Telescope* (*HST*) Paschen-α survey toward the inner part of the CMZ (see the black contour in Figures 3–5; Wang et al. 2010; Dong et al. 2011). The detection of Pa-α emission toward a compact source suggests thermal emission, which could be from UC H II regions but could also arise from evolved stars and planetary nebulae (see discussion in Section 4.1.3).

Dong et al. (2011) compiled Pa-α emitting source catalogs. Sources in the catalogs are point like with a resolution of $0\farcs2$ from the *HST* observations, and are mostly evolved high-mass stars as suggested by the authors. The Pa-α emission associated

Table 4
Properties of CH_3OH Masers

ID	R.A. and Decl. (J2000)	v_{peak}[a] (km s^{-1})	F_{peak}[a,b] (Jy per channel)	F_{int}[b] (Jy km s^{-1})	Refs.
M1	17:47:24.74, −28:21:43.16	68.17	21.22	50.82	H95, C96
M2	17:47:18.66, −28:22:10:17	71.68	0.06	0.40	this work
M3	17:47:19.79, −28:22:12:64	73.44	0.05	0.24	this work
M4	17:47:19.27, −28:22:14:50	73.44	0.77	4.79	H95, C96
M5	17:47:19.54, −28:22:31:98	60.79	0.08	0.11	H95, C96
M6	17:47:20.04, −28:22:40:98	58.34	8.45	6.01	H95, C96
M7	17:47:18.65, −28:22:54:28	70.63	37.64	33.88	H95, C96
M8	17:47:19.87, −28:23:01:04	55.17	0.35	0.37	H95, C96
M9	17:47:20.15, −28:23:06:02	66.76	0.16	0.19	this work
M10	17:47:20.04, −28:23:12:46	60.44	4.55	2.66	H95, C96
M11	17:47:20.05, −28:23:46:42	50.61	5.02	10.05	H95, C96
M12	17:47:21.11, −28:24:17:95	48.15	17.71	16.02	H95, C96
M13	17:47:18.65, −28:24:24:63	49.55	56.06	102.11	H95, C96
M14	17:47:22.04, −28:24:42:33	50.96	3.46	3.34	H95, C96
M15	17:46:47.07, −28:32:06:86	27.90	2.00	4.80	C09
M16	17:46:21.41, −28:35:39:02	37.03	0.33	0.43	C96
M17	17:46:07.68, −28:45:20:48	49.33	2.94	5.31	C96
M18	17:45:35.00, −29:23:15:05	29.69	0.20	0.15	this work
M19	17:45:39.86, −29:23:23:21	21.96	0.12	0.15	this work
M20	17:45:39.07, −29:23:29:96	19.50	41.23	64.62	C96
M21	17:44:41.31, −29:27:58:32	−55.66	0.24	0.24	this work
M22	17:44:40.18, −29:28:12:28	−56.72	0.98	1.91	C96
M23	17:44:40.61, −29:28:15:28	−46.88	63.92	61.13	C96

Notes.
[a] For masers with multiple velocity components along the line of sight, V_{lsr}, and the flux of the strongest peak is listed.
[b] Fluxes have been corrected for primary beam response.
References. C96: Caswell (1996). C09: Caswell (2009). H95: Houghton & Whiteoak (1995).

Table 5
Properties of H_2CO Masers

ID	R.A. and Decl. (J2000)	v_{peak}[a] (km s^{-1})	F_{peak}[a,b] (Jy per channel)	F_{int}[b] (Jy km s^{-1})	Refs.
F1	17:47:19.86, −28:22:12:82	75.15	1.18[c]	0.91[c]	M94
F2	17:47:20.14, −28:23:04:23	50.41	0.09[c]	0.66[c]	M94
F3	17:47:20.05, −28:23:46:58	49.93	0.21	0.70	M94
F4	17:47:19.58, −28:23:49:64	48.96	0.18	0.38	M94
F5	17:47:18.65, −28:24:24:57	48.96	0.29[c]	0.64[c]	M94
F6	17:46:21.40, −28:35:39:09	36.96	0.88	1.54	G15
F7	17:44:40.18, −29:28:11:96	−43.03	0.09	0.13	this work
F8	17:44:40.60, −29:28:15:10	−54.19	0.18	0.44	this work

Notes.
[a] For masers with multiple velocity components along the line of sight, V_{lsr}, and flux of the strongest peak is listed.
[b] Fluxes have been corrected for primary beam response.
[c] Significant absorption is superimposed with maser emission (Figure 7); therefore, reported fluxes are lower limits.
References. G15: Ginsburg et al. (2015). M94: Mehringer et al. (1994).

with our compact sources tends to be diffuse and is not cataloged by Dong et al. (2011). Therefore, we compare directly with the Pa-α image instead of the catalogs. Among the 104 sources identified in Section 3.2, 28 are within the observed area of *HST*. Sixteen sources have Pa-α emission counterparts. Nine of them have spectral indices <-0.1 after taking systematic and fitting uncertainties into account. This again demonstrates the limitation of using spectral indices to infer the nature of the continuum sources.

Second, we compare with H II region catalogs, which are mostly based on infrared emission, and in some cases with supplemental radio continuum data. Giveon et al. (2005) have compiled a catalog based on MAGPIS 5 GHz continuum emission (4″ resolution; Becker et al. 1994) and *Midcourse Space Experiment* infrared emission. However, after cross-matching with our *C*-band images, we find that all of their identified H II regions are diffuse structures (e.g., Sgr B2(M)), and none matches with the compact sources we identify. The other H II region catalog compiled by Anderson et al. (2014) makes use of the *Wide-Field infrared Survey Explorer* (*WISE*) data (∼6″ resolution at the shorter wavelength bands) and is suggested to be the most complete one to date. We search for

H II regions in the catalog within a radius of 6″ around our compact sources, and find three matches, which are marked in Table 3.

Third, we compare with the YSO catalogs of Yusef-Zadeh et al. (2009) and An et al. (2011), both based on the *Spitzer* infrared data. The Yusef-Zadeh et al. (2009) catalog used 24 μm data (∼6″ resolution) to identify 559 YSO candidates, but may be contaminated by more evolved objects such as main-sequence stars (Koepferl et al. 2015), and several candidates were indeed ruled out later by An et al. (2011) through infrared spectra (e.g., the one associated with C75, SSTGC374813). It also includes 33 Extended Green Objects (EGOs), a class of objects that are supposed to be associated with massive YSOs (Cyganowski et al. 2008). We cross-match between the YSO candidates and our compact source catalog with a search radius of 6″, and find that eight sources (C10, C23, C56, C63, C72, C75, C89, and C97) are coincident with YSO candidates. The EGOs are usually spatially extended, so we use a larger search radius of 9″ (characteristic radius of EGOs; Cyganowski et al. 2008) and find four matches (C23, C82/C83, and C103), which have been classified as UC H II regions given correlations with class II CH_3OH masers. The An et al. (2011) catalog is smaller, with 16 YSOs and 19 possible YSOs that are selected from the *Spitzer* Infrared Array Camera images (∼2″ resolution) and then spectroscopically classified. We find only one match with a search radius of 2″: C37 matches with a possible YSO. All of these associations are marked in Table 3.

Fourth, we compare with the *Herschel* column densities (Battersby et al. 2011; C. Battersby et al. 2019, in preparation). UC H II regions are deeply embedded in molecular gas, and therefore should be associated with high column densities, although sources of other nature can be projected onto this area by chance. We apply a column density threshold of 5×10^{22} cm^{-2} (the lowest contour level in Figures 2–5) and search for compact sources above it. This column density threshold is chosen to be the upper limit of the foreground column density toward Sgr B2 (Ginsburg et al. 2018; C. Battersby et al. 2019, in preparation), so any emission above it is very likely associated with true gas components in the CMZ while that below it could be in the background. Thirty out of the 104 sources are found above the column density threshold and marked in Table 3.

4.1.3. Correlation with Other Surveys that Argue Against UC H II Regions

Apart from star formation in molecular clouds, various alternative processes may contribute to the observed compact continuum emission. Here we compare our identified compact sources with studies that target other objects, including field stars, star clusters, and pulsars, to exclude potential contamination from those objects in our detections.

First, the two young massive star clusters in the CMZ, the Arches and the Quintuplet, are known to host high-mass stars with strong stellar winds and free–free emission that can be detected in the radio continuum. We compare with the VLA multifrequency observations of Lang et al. (2005) and find that C41 is likely associated with a stellar member (source AR1 in the Arches cluster; Lang et al. 2005).

Second, field stars may ionize surrounding gas and create H II regions. One example is the Sgr A–H H II regions, scattered in projection between Sgr A* and the Arches cluster (Yusef-Zadeh & Morris 1987b; Lang et al. 2001), most of which are likely associated with field stars (Dong et al. 2017; Hankins et al. 2017). We compare with the VLA multi-frequency observations of Lang et al. (2001) and Stratospheric Observatory for Infrared Astronomy (SOFIA) mid-infrared observations of Hankins et al. (2019) toward this area, and find that C44, C45, and C46 are spatially coincident with three known H II regions (H13, H12, and H11) within a radius of 1″, which may be powered by massive field stars. We also compare with Galactic Center-wide studies of massive field stars (Mauerhan et al. 2010a, 2010b; Dong et al. 2015) and find one match, C51, with a star in Mauerhan et al. (2010b) within a radius of 1″.

Third, pulsars, X-ray binaries, stellar winds from massive stars, and background active galactic nuclei (AGNs) can contribute to radio continuum emission. These targets are usually seen as point sources in X-ray emission, while UC H II regions may present diffuse X-ray emission ($\gtrsim$0.2 pc, 5″ at the distance of the CMZ; e.g., Tsujimoto et al. 2006) and therefore can be distinguished. We cross-match with *Chandra* X-ray point source catalogs of Muno et al. (2006, 2009) and Zhu et al. (2018) with a search radius of 1″, and find the following matches: C1, C5, C25, C41, C48, C51, C55, C60, C63, and C86. Among them, C41 and C51 likely originate from stellar winds of massive stars as discussed above. The other eight sources are unlikely to be UC H II regions either given their association with X-ray point sources.

Lastly, evolved stars (e.g., planetary nebulae, PNe; Mira variables) have thermal continuum emission that can be detected in radio frequencies. We cross-match with the PNe database of Parker et al. (2016) and find that C47 (also known as N1; Yusef-Zadeh & Morris 1987a) is consistent with a known PN. In addition, C43 is spatially coincident with a Mira variable from the survey of Glass et al. (2001).

Some sources listed above are already unlikely to be UC H II regions given negative spectral indices or the lack of correlations in Section 4.1.2, but we do find a few sources that meet two or more criteria in Section 4.1.2 yet still are of nature other than UC H II regions (e.g., C41, C43, C47, C51, C86). This is expected because massive stars or evolved stars can present infrared and Pa-α emission and positive spectral indices similar to UC H II regions, and may be located adjacent to massive clouds where they are born (especially for the short-lived massive stars), which explain the correlations found in Section 4.1.2. We list all counterparts discussed in this section in Table 3.

4.1.4. UC H II Region Candidates and the Nature of the Other Sources

The above results demonstrate that a single criterion (spectral index, Pa-α emission, *WISE* H II regions, *Spitzer* YSOs, or column densities) is insufficient to determine the nature of a compact source. Therefore, we combine evidence from different observations: if at least two of the criteria discussed in Section 4.1.2 are met, then the compact source is taken as a UC H II region candidate. In addition, if the source is found to have any counterpart in Section 4.1.3, it is immediately excluded to be a UC H II region. As shown in Table 3, we have 12 candidates in addition to the five confirmed cases.

Distances of the UC H II candidates are still unknown, and they could be in the foreground or background instead of lying within the CMZ. Two cases are C82 and C83, which appear to be associated with the CH_3OH maser M20 that is in the foreground (see Section 3.3). Observations of recombination

lines toward these candidates can both confirm the nature of the continuum emission and yield velocity information that can be used to infer the correlation with the CMZ along the line of sight.

Of the 87 sources that are not identified as UC H II or candidates, 15 have counterparts such as massive cluster or field stars, X-ray point sources (pulsars, X-ray binaries, or AGNs), or evolved stars. The remaining 72 sources are also likely massive field stars, evolved stars, pulsars, or extragalactic sources instead of embedded UC H II regions, given their negative spectral indices and lack of correlation with high column densities. At least one of these sources, C96, presents a double-lobe morphology, which may suggest radio lobes associated with AGNs. A recent VLA 5.5 GHz survey of the GOODS-North field detected 94 sources (including both star-forming galaxies and AGNs) in an area of 150 arcmin^2 (Guidetti et al. 2017), and three of them are above the flux threshold of 0.56 mJy (corresponding to five times the median rms of our observations). If this detection rate is representative for background sources of extragalactic origins, in the area of 1100 arcmin^2 covered by our observations, 22 extragalactic sources are expected. Therefore, we expect a substantial fraction of the 72 sources to be background galaxies or AGNs. Future observations of recombination lines as well as radio continuum at different wavelengths will help clarify their nature.

4.2. Implications for Star Formation in the CMZ

4.2.1. Class II CH_3OH Masers and High-mass Star Formation

The 6.668 GHz CH_3OH maser is one of the radiatively excited class II CH_3OH masers, which are suggested to uniquely trace high-mass star formation (Menten 1991; Ellingsen 2006; Xu et al. 2008; Breen et al. 2013). Therefore, it is not surprising that most of the 23 detected CH_3OH masers are associated with known high-mass star formation regions. Among them, 12 out of the 14 CH_3OH masers in Sgr B2 are associated with UC/HC H II regions (Gaume et al. 1995; De Pree et al. 2015) or massive YSOs (Ginsburg et al. 2018), while M2 and M11 do not have H II region or YSO counterparts within 1″ (see next paragraph). The three masers in the Dust Ridge clouds (M15, M16, and M17) are associated with (UC) H II regions or massive YSOs (Immer et al. 2012a; Walker et al. 2018; Lu et al. 2019). The three masers in Sgr C (M12, M22, and M23) are coincident with three (UC) H II regions, respectively (Kendrew et al. 2013; Lu et al. 2019). M20 in the Pillar cloud is also coincident with a massive YSO traced by an EGO (Yusef-Zadeh et al. 2009; Chambers et al. 2011, 2014), although it is likely in the foreground, not in the CMZ.

Four masers are not clearly associated with any known high-mass star formation activity. One of them is the previously identified maser M11 in Sgr B2, which is 5″ offset from the H II region Sgr B2 H (or Sgr B2 South; Gaume et al. 1995) and is spatially associated with the H_2CO maser F3. The other three are newly detected—M2 in Sgr B2, and M18 and M19 in the Pillar cloud, which are likely in the foreground together with the YSO associated with M20 given their similar V_{lsr}. Future high-resolution ($\lesssim$1″) observations in the radio and submillimeter bands will help in the search for gas components associated with these masers.

The 6.668 GHz CH_3OH masers are rarer in the CMZ relative to the 22.235 GHz H_2O masers (Walsh et al. 2011; Lu et al. 2019) and are concentrated in five high-mass star-forming regions (excluding the foreground Pillar cloud). For example, in Lu et al. (2019), we detected numerous H_2O masers in a high-mass star-forming region, the 20 km s^{-1} cloud, but so far no class II CH_3OH maser has been detected toward this region.

The CH_3OH molecule itself is abundant in the CMZ (Jones et al. 2013); therefore, the relative dearth of the 6.668 GHz CH_3OH masers does not stem from the chemistry of interstellar gas. It is more likely due to the excitation condition of this maser, which is related to evolutionary phases or protostellar masses of the high-mass star formation activities.

Among the clouds where class II CH_3OH masers are detected, Sgr C, Dust Ridge clouds c/e, and the Brickette cloud have infrared sources embedded in molecular gas and spatially associated with the masers (Immer et al. 2012a; Kendrew et al. 2013; Walker et al. 2018; Lu et al. 2019). For Sgr B2, the infrared emission is usually saturated in observations, but we find massive YSO or UC H II region counterparts for most of the masers (Gaume et al. 1995; De Pree et al. 2015; Ginsburg et al. 2018). Therefore, these clouds may provide strong radiation from protostars to excite the CH_3OH masers. The 20 km s^{-1} cloud, on the other hand, does not contain embedded infrared sources corresponding to the star formation signatures traced by H_2O masers and dense cores (Lu et al. 2019). It may be at an even earlier evolutionary phase, or may not harbor protostars above a certain mass threshold that have strong-enough radiation to excite class II CH_3OH masers.

4.2.2. H_2CO Masers and High-mass Star Formation

The 4.830 GHz H_2CO maser has been detected in eight locations in the Galaxy, all of which are high-mass star-forming regions (Ginsburg et al. 2015 and references therein). Our observations reveal Sgr C (specifically, the two (UC) H II regions in it) as the ninth region with H_2CO maser detection, which is also a high-mass star-forming region. This may suggest that the H_2CO maser is exclusively associated with high-mass star formation, same as the class II CH_3OH maser.

Except for one H_2CO maser, F4, the H_2CO masers we detect are always projected within 1″ around class II CH_3OH masers or associated with the same (UC) H II region. This high frequency of coexistence between the two types of masers suggests the excitation condition of the H_2CO maser is similar to but is more stringent than that of the class II CH_3OH maser. For example, the luminosity threshold of YSOs to excite the H_2CO maser may be higher, or the time period that allows the excitation of the H_2CO maser may be shorter. Exactly how the H_2CO maser is excited is still unclear (e.g., van der Walt 2014).

Ginsburg et al. (2015) discussed the relative prevalence of H_2CO masers in the CMZ as compared to the Galactic disk, and our new detections reinforce this statement (three regions in the CMZ versus six in the Galactic disk). As suggested by Ginsburg et al. (2015), this may suggest that the H_2CO masers trace a very short period in high-mass star formation, and the three occurrences of H_2CO masers in the CMZ indicate an ongoing burst of star formation, or this may be related to the high abundance of gas-phase H_2CO at small spatial scales ($\sim$100 au) in the CMZ.

4.2.3. Inefficient High-mass Star Formation in the CMZ

Overall, we find evidence of early-phase high-mass star formation traced by class II CH_3OH masers and embedded UC

Table 6
Summary of High-mass Star Formation Indicators

Regions	No. of UC/HC H II Regions	Refs. for UC/HC H II Regions	No. of Class II CH_3OH Masers	No. of Unique Indicators[a]	SFR[b] (10^{-3} $M_\odot$ yr^{-1})
Sgr B2	41	G95, D15	14	50	21.5
Dust Ridge cloud e	1	L19	1	1	0.4
Dust Ridge cloud c	1	this work	1	1	0.4
Brickette	0	⋯	1	1	0.4
The 50 km s^{-1} cloud	1	E83, M11, L19	0	1	0.4
The 20 km s^{-1} cloud	1	L19	0	1	0.4
Sgr C	2	F00, L19, this work	3	3	1.3
Total	47	⋯	20	58	24.9

Notes.
[a] Class II CH_3OH masers spatially associated with known UC/HC H II regions are excluded. In Sgr B2: M6—source Z10.24 (Gaume et al. 1995). M7—source Y (Gaume et al. 1995). M8—source B (Gaume et al. 1995). M9—sources F10.33/F10.35/F10.37/F10.39 (Gaume et al. 1995). M10—source D (Gaume et al. 1995). In Dust Ridge cloud e: M15—source H1 (Lu et al. 2019). In Dust Ridge cloud c: M16—C23 (this work). In Sgr C: M21—C102 (this work). M22—C103 (this work).
[b] We assume each unique high-mass star formation indicator corresponds to a high-mass protostar of >10 $M_\odot$, thus representing a total stellar mass of 129 $M_\odot$ (see Appendix D of Lu et al. 2019). The SFR is derived by dividing the total stellar mass in the considered region by the characteristic timescale of 0.3 Myr.
References. D15: De Pree et al. (2015). E83: Ekers et al. (1983). F00: Forster & Caswell (2000). G95: Gaume et al. (1995). L19: Lu et al. (2019). M11: Mills et al. (2011).

H II regions only toward five isolated regions in the inner CMZ: Sgr B2, Sgr C, Dust Ridge cloud c, Dust Ridge cloud e, and the Brickette. All of them have been known to form high-mass stars (Immer et al. 2012a; Kendrew et al. 2013; Walker et al. 2015, 2018; Ginsburg et al. 2018; Lu et al. 2019). There are two other high-mass star-forming clouds, the 20 km s^{-1} cloud and the 50 km s^{-1} cloud (Mills et al. 2011; Lu et al. 2015, 2019), where we do not detect any class II CH_3OH masers or UC H II regions. Therefore, we are not able to confirm any new high-mass star-forming clouds in the CMZ through our observations, and all currently known high-mass star-forming regions in the inner CMZ are confined in seven clouds. A brief summary of the star formation indicators can be found in Table 6.

Krumholz & McKee (2008) suggested a column density threshold for high-mass star formation of 2×10^{23} cm^{-2}. Among the seven high-mass star-forming clouds, Dust Ridge cloud c, the Brickette, and the 50 km s^{-1} cloud have column densities below the threshold in the *Herschel* maps (Figures 3 & 4), although smaller regions embedded in them above the threshold have been found (e.g., Walker et al. 2018; Lu et al. 2019). There are three clouds lying above the threshold but showing no signatures of high-mass star formation in our observations and previous studies: G0.253+0.016, and Dust Ridge clouds d and f. G0.253+0.016 has been proven to be genuinely lacking star formation (Kauffmann et al. 2013; Longmore et al. 2013b; Mills et al. 2015; Rathborne et al. 2015), while Dust Ridge clouds d and f do not show signs of active ongoing star formation either (Walker et al. 2018; Barnes et al. 2019; Lu et al. 2019). The strong solenoidally driven turbulence may increase the density threshold for star formation, and therefore inhibit star formation in the three clouds despite their high column densities (Federrath et al. 2016; Dale et al. 2019; Henshaw et al. 2019; Kruijssen et al. 2019).

If we simply consider the total molecular gas mass in the inner CMZ of $\sim 10^7$ $M_\odot$ with a mean density of $\sim 10^4$ cm^{-3} (Longmore et al. 2013a), the expected SFR based on the dense gas star formation relation extrapolated from nearby clouds (Lada et al. 2010) is 0.46 $M_\odot$ yr^{-1}. Further assuming a typical timescale of 0.3 Myr for the star formation activities traced by UC H II regions and class II CH_3OH masers (Davies et al. 2011) and a canonical multiple-power-law initial mass function between 0.01 $M_\odot$ and 150 $M_\odot$ (Kroupa 2001), we expect to find between 940 and 1069 high-mass protostars above 10–11 $M_\odot$ in this region (see Appendix D of Lu et al. 2019). Here, the threshold of 10–11 $M_\odot$ corresponds to the detection limit of the continuum emission (see Section 3.2). However, even after taking into account maser variability or multiplicity of protostars that may result in an underestimate of a factor of 2 in observations of star formation indicators, this still outnumbers the observed UC H II regions and class II CH_3OH masers combined in the inner CMZ by an order of magnitude (58 in total; see Table 6). Alternatively, we compare the SFR based on the observed star formation indicators with that expected by the dense gas star formation relation. We assume each UC H II region or class II CH_3OH maser corresponds to a high-mass protostar above 10 $M_\odot$, and follow the methods in Appendix D of Lu et al. (2019) to estimate the SFR. The results are listed in Table 6, and the total SFR in the surveyed area, 0.025 $M_\odot$ yr^{-1}, is an order of magnitude smaller than the 0.46 $M_\odot$ yr^{-1} that is expected by the dense gas star formation relation. Our observations therefore strengthen the conclusion that star formation in the CMZ is suppressed by about a factor of 10 than expected from the dense gas star formation relation, which has been drawn from observations of more evolved phases of star formation (in the last several Myr; Longmore et al. 2013a; Barnes et al. 2017). Furthermore, because our observations trace very early phases of star formation deeply embedded in molecular clouds, the results imply that the incipient star formation (in the last ~0.3 Myr) in the CMZ remains inefficient, and that any impending, next burst of star formation has not yet begun (Krumholz & Kruijssen 2015).

Finally, in spite of the overall inefficient star formation in the CMZ, we confirm that Sgr C is actively forming stars. Our new detections of H_2CO masers toward Sgr C make it one of the most maser-rich regions in the Galaxy, similar to Sgr B2 and Dust Ridge cloud c. So far, H_2O (Caswell et al. 1983; Walsh et al. 2011), OH (Caswell 1998; Cotton & Yusef-Zadeh 2016), class II CH_3OH, and H_2CO masers have been detected toward the two (UC) H II regions in Sgr C. Outside of the two (UC) H II

regions, a total of 14 H_2O masers have been detected throughout the Sgr C cloud (Lu et al. 2019), one of which is spatially coincident with the class II CH_3OH maser M21 (the H_2O maser W8; see Figure 4 of Lu et al. 2019). Therefore, at least three positions in Sgr C are forming high-mass stars, creating a variety of masers and UC H II regions, while more than 10 other positions are likely forming low- to intermediate-mass stars. In fact, Sgr C is one of the few CMZ clouds that show SFRs consistent with the dense gas star formation relation, along with Sgr B2 and Dust Ridge cloud c (Kauffmann et al. 2017a; Lu et al. 2019). The active star formation in Sgr C may be related to its high fragmentation level and large fraction of gas mass confined in gravitationally bound cores, as opposed to the lack of fragmentation in most other CMZ clouds (e.g., Kauffmann et al. 2017b; C. Battersby et al. 2019, in preparation; H. Hatchfield et al. 2019, in preparation), though the origin of this unique gas structure is unclear. It may be a combined effect of self-gravity, impact of a nearby 10 pc scale H II region (e.g., gas collapse triggered by expanding ionization fonts of the H II region; Liszt & Spiker 1995; Lang et al. 2010), and global gas dynamics in the CMZ (e.g., gas compression induced by the tidal field of the CMZ; Kruijssen et al. 2015, 2019; Jeffreson et al. 2018; Dale et al. 2019).

5. Conclusions

We report new VLA observations of the *C*-band continuum emission, 6.668 GHz CH_3OH masers, and 4.830 GHz H_2CO masers at $\sim 1''$ resolution toward the inner part of the CMZ. We use these data to search for high-mass star formation at early evolutionary phases in the CMZ. The continuum observation is complete to free–free emission from stars above 10–11 $M_\odot$ throughout the inner 200 pc of the CMZ except for small regions around bright continuum sources in Sgr B2 and Sgr A. Using the continuum emission, we confirm five UC H II regions, and find 12 UC H II region candidates whose nature needs to be verified in the future. We detect 23 CH_3OH masers and eight H_2CO masers, among which six and two are new detections, respectively.

Despite the new UC H II region candidates and the new detections of masers, we do not find more signatures of ongoing high-mass star formation than previously known in the CMZ. Our observations suggest that current high-mass star formation in the CMZ is concentrated in a few isolated regions with high column densities ($\gtrsim 10^{23}$ cm^{-2}; including the 20 km s^{-1} cloud, the 50 km s^{-1} cloud, Dust Ridge clouds c and e, Brickette, Sgr B2, and Sgr C). Combined with previous studies that focus on more evolved phases (in the last several megayears) of star formation in the CMZ and find a star formation efficiency at least 10 times lower than expected by the dense gas star formation relation, our results indicate that star formation at early evolutionary phases (in the last $\sim$0.3 Myr) in the CMZ remains inefficient, and that if there is any impending, next burst of star formation, it has not yet begun.

We thank the referee, Daniel Wang, for helpful comments. We thank NRAO staff for their support with the VLA observations and data reduction. This work was supported by JSPS KAKENHI grant No. JP18K13589. C.B. was supported by the National Science Foundation under grant No. 1816715. J.M.D.K. gratefully acknowledges funding from the German Research Foundation (DFG) in the form of an Emmy Noether Research Group (grant No. KR4801/1-1) and from the European Research Council (ERC) under the European Union's Horizon 2020 research and innovation programme via the ERC Starting Grant MUSTANG (grant agreement number 714907). K.W. acknowledges support by the National Key Research and Development Program of China (2017YFA0402702), the National Science Foundation of China (11973013, 11721303), and the starting grant at the Kavli Institute for Astronomy and Astrophysics, Peking University (7101502016). This research made use of Astropy, a community-developed core Python package for Astronomy (Astropy Collaboration et al. 2013), and APLpy, an open-source plotting package for Python (Robitaille & Bressert 2012). Data analysis was in part carried out on the open-use data analysis computer system at the Astronomy Data Center (ADC) of the National Astronomical Observatory of Japan. This research has made use of NASA's Astrophysics Data System. This research has made use of the SIMBAD database and the VizieR catalog access tool, operated at CDS, Strasbourg, France.

Facility: VLA.

Software: CASA (McMullin et al. 2007), SExtractor (Bertin & Arnouts 1996), BLOBCAT (Hales et al. 2012), APLpy (Robitaille & Bressert 2012), Astropy (Astropy Collaboration et al. 2013).

ORCID iDs

Xing Lu (吕行) https://orcid.org/0000-0003-2619-9305
Elisabeth A. C. Mills https://orcid.org/0000-0001-8782-1992
Adam Ginsburg https://orcid.org/0000-0001-6431-9633
Natalie Butterfield https://orcid.org/0000-0002-4013-6469
Cara Battersby https://orcid.org/0000-0002-6073-9320
Steven N. Longmore https://orcid.org/0000-0001-6353-0170
Qizhou Zhang https://orcid.org/0000-0003-2384-6589
John Bally https://orcid.org/0000-0001-8135-6612
Jürgen Ott https://orcid.org/0000-0001-8224-1956

References

An, D., Ramírez, S. V., Sellgren, K., et al. 2011, ApJ, 736, 133
Anderson, L. D., Bania, T. M., Balser, D. S., et al. 2014, ApJS, 212, 1
Ao, Y., Henkel, C., Menten, K. M., et al. 2013, A&A, 550, A135
Astropy Collaboration, Robitaille, T. P., Tollerud, E. J., et al. 2013, A&A, 558, A33
Bally, J., Stark, A. A., Wilson, R. W., & Henkel, C. 1987, ApJS, 65, 13
Barnes, A. T., Longmore, S. N., Avison, A., et al. 2019, MNRAS, 486, 283
Barnes, A. T., Longmore, S. N., Battersby, C., et al. 2017, MNRAS, 469, 2263
Battersby, C., Bally, J., Ginsburg, A., et al. 2011, A&A, 535, A128
Becker, R. H., White, R. L., Helfand, D. J., & Zoonematkermani, S. 1994, ApJS, 91, 347
Bertin, E., & Arnouts, S. 1996, A&AS, 117, 393
Bihr, S., Johnston, K. G., Beuther, H., et al. 2016, A&A, 588, A97
Breen, S. L., Ellingsen, S. P., Contreras, Y., et al. 2013, MNRAS, 435, 524
Butterfield, N., Lang, C. C., Morris, M., Mills, E. A. C., & Ott, J. 2018, ApJ, 852, 11
Caswell, J. L. 1996, MNRAS, 283, 606
Caswell, J. L. 1998, MNRAS, 297, 215
Caswell, J. L. 2009, PASA, 26, 454
Caswell, J. L., Batchelor, R. A., Forster, J. R., & Wellington, K. J. 1983, AuJPh, 36, 401
Caswell, J. L., Fuller, G. A., Green, J. A., et al. 2010, MNRAS, 404, 1029
Chambers, E. T., Yusef-Zadeh, F., & Ott, J. 2014, A&A, 563, A68
Chambers, E. T., Yusef-Zadeh, F., & Roberts, D. 2011, ApJ, 733, 42
Churchwell, E. 2002, ARA&A, 40, 27
Cotton, W. D., & Yusef-Zadeh, F. 2016, ApJS, 227, 10
Cyganowski, C. J., Whitney, B. A., Holden, E., et al. 2008, AJ, 136, 2391
Dale, J. E., Kruijssen, J. M. D., & Longmore, S. N. 2019, MNRAS, 486, 3307

Davies, B., Hoare, M. G., Lumsden, S. L., et al. 2011, MNRAS, 416, 972
de Pree, C. G., Gaume, R. A., Goss, W. M., & Claussen, M. J. 1995, ApJ, 451, 284
de Pree, C. G., Gaume, R. A., Goss, W. M., & Claussen, M. J. 1996, ApJ, 464, 788
De Pree, C. G., Peters, T., Mac Low, M. M., et al. 2015, ApJ, 815, 123
Dong, H., Lacy, J. H., Schödel, R., et al. 2017, MNRAS, 470, 561
Dong, H., Mauerhan, J., Morris, M. R., Wang, Q. D., & Cotera, A. 2015, MNRAS, 446, 842
Dong, H., Wang, Q. D., Cotera, A., et al. 2011, MNRAS, 417, 114
Ekers, R. D., van Gorkom, J. H., Schwarz, U. J., & Goss, W. M. 1983, A&A, 122, 143
Ellingsen, S. P. 2006, ApJ, 638, 241
Federrath, C., Rathborne, J. M., Longmore, S. N., et al. 2016, ApJ, 832, 143
Forster, J. R., & Caswell, J. L. 2000, ApJ, 530, 371
Gaia Collaboration, Brown, A. G. A., Vallenari, A., et al. 2018, A&A, 616, A1
Gaume, R. A., Claussen, M. J., de Pree, C. G., Goss, W. M., & Mehringer, D. M. 1995, ApJ, 449, 663
Ginsburg, A., Bally, J., Barnes, A., et al. 2018, ApJ, 853, 171
Ginsburg, A., Henkel, C., Ao, Y., et al. 2016, A&A, 586, A50
Ginsburg, A., Walsh, A., Henkel, C., et al. 2015, A&A, 584, L7
Giveon, U., Becker, R. H., Helfand, D. J., & White, R. L. 2005, AJ, 129, 348
Glass, I. S., Matsumoto, S., Carter, B. S., & Sekiguchi, K. 2001, MNRAS, 321, 77
Gravity Collaboration, Abuter, R., Amorim, A., et al. 2018, A&A, 615, L15
Guidetti, D., Bondi, M., Prandoni, I., et al. 2017, MNRAS, 471, 210
Hales, C. A., Murphy, T., Curran, J. R., et al. 2012, MNRAS, 425, 979
Hankins, M. J., Lau, R. M., Mills, E. A. C., Morris, M. R., & Herter, T. L. 2019, ApJ, 877, 22
Hankins, M. J., Lau, R. M., Morris, M. R., & Herter, T. L. 2017, ApJ, 837, 79
Henshaw, J. D., Ginsburg, A., Haworth, T. J., et al. 2019, MNRAS, 485, 2457
Houghton, S., & Whiteoak, J. B. 1995, MNRAS, 273, 1033
Immer, K., Menten, K. M., Schuller, F., & Lis, D. C. 2012a, A&A, 548, A120
Immer, K., Schuller, F., Omont, A., & Menten, K. M. 2012b, A&A, 537, A121
Jeffreson, S. M. R., Kruijssen, J. M. D., Krumholz, M. R., & Longmore, S. N. 2018, MNRAS, 478, 3380
Jones, P. A., Burton, M. G., Cunningham, M. R., Tothill, N. F. H., & Walsh, A. J. 2013, MNRAS, 433, 221
Kauffmann, J., & Pillai, T. 2010, ApJL, 723, L7
Kauffmann, J., Pillai, T., & Zhang, Q. 2013, ApJL, 765, L35
Kauffmann, J., Pillai, T., Zhang, Q., et al. 2017a, A&A, 603, A89
Kauffmann, J., Pillai, T., Zhang, Q., et al. 2017b, A&A, 603, A90
Kendrew, S., Ginsburg, A., Johnston, K., et al. 2013, ApJL, 775, L50
Koepferl, C. M., Robitaille, T. P., Morales, E. F. E., & Johnston, K. G. 2015, ApJ, 799, 53
Krieger, N., Ott, J., Beuther, H., et al. 2017, ApJ, 850, 77
Kroupa, P. 2001, MNRAS, 322, 231
Kruijssen, J. M. D., Dale, J. E., & Longmore, S. N. 2015, MNRAS, 447, 1059
Kruijssen, J. M. D., Dale, J. E., Longmore, S. N., et al. 2019, MNRAS, 484, 5734
Kruijssen, J. M. D., Longmore, S. N., Elmegreen, B. G., et al. 2014, MNRAS, 440, 3370
Krumholz, M. R., & Kruijssen, J. M. D. 2015, MNRAS, 453, 739
Krumholz, M. R., Kruijssen, J. M. D., & Crocker, R. M. 2017, MNRAS, 466, 1213
Krumholz, M. R., & McKee, C. F. 2008, Natur, 451, 1082
Lada, C. J., Lombardi, M., & Alves, J. F. 2010, ApJ, 724, 687
Lang, C. C., Goss, W. M., Cyganowski, C., & Clubb, K. I. 2010, ApJS, 191, 275
Lang, C. C., Goss, W. M., & Morris, M. 2001, AJ, 121, 2681
Lang, C. C., Johnson, K. E., Goss, W. M., & Rodríguez, L. F. 2005, AJ, 130, 2185
Lazio, T. J. W., & Cordes, J. M. 2008, ApJS, 174, 481
Liszt, H. S., & Spiker, R. W. 1995, ApJS, 98, 259
Lo, K. Y., & Claussen, M. J. 1983, Natur, 306, 647
Longmore, S. N., Bally, J., Testi, L., et al. 2013a, MNRAS, 429, 987
Longmore, S. N., Kruijssen, J. M. D., Bally, J., et al. 2013b, MNRAS, 433, L15
Lu, X., Zhang, Q., Kauffmann, J., et al. 2015, ApJL, 814, L18
Lu, X., Zhang, Q., Kauffmann, J., et al. 2017, ApJ, 839, 1
Lu, X., Zhang, Q., Kauffmann, J., et al. 2019, ApJ, 872, 171
Ludovici, D. A., Lang, C. C., Morris, M. R., et al. 2016, ApJ, 826, 218
Mauerhan, J. C., Cotera, A., Dong, H., et al. 2010a, ApJ, 725, 188
Mauerhan, J. C., Muno, M. P., Morris, M. R., Stolovy, S. R., & Cotera, A. 2010b, ApJ, 710, 706
McMullin, J. P., Waters, B., Schiebel, D., Young, W., & Golap, K. 2007, in ASP Conf. Ser. 376, Astronomical Data Analysis Software and Systems XVI, ed. R. A. Shaw, F. Hill, & D. J. Bell (San Francisco, CA: ASP), 127
Mehringer, D. M., Goss, W. M., & Palmer, P. 1994, ApJ, 434, 237
Mehringer, D. M., Palmer, P., & Goss, W. M. 1995, ApJS, 97, 497
Mehringer, D. M., Palmer, P., Goss, W. M., & Yusef-Zadeh, F. 1993, ApJ, 412, 684
Meidt, S. E., Leroy, A. K., Rosolowsky, E., et al. 2018, ApJ, 854, 100
Menten, K. 1991, in ASP Conf. Ser. 16, Atoms, Ions and Molecules: New Results in Spectral Line Astrophysics, ed. A. D. Haschick & P. T. P. Ho (San Francisco, CA: ASP), 119
Mezger, P. G., Smith, L. F., & Churchwell, E. 1974, A&A, 32, 269
Mills, E., Morris, M. R., Lang, C. C., et al. 2011, ApJ, 735, 84
Mills, E. A. C., Butterfield, N., Ludovici, D. A., et al. 2015, ApJ, 805, 72
Molinari, S., Swinyard, B., Bally, J., et al. 2010, A&A, 518, L100
Muno, M. P., Bauer, F. E., Baganoff, F. K., et al. 2009, ApJS, 181, 110
Muno, M. P., Bauer, F. E., Bandyopadhyay, R. M., & Wang, Q. D. 2006, ApJS, 165, 173
Parker, Q. A., Bojičić, I. S., & Frew, D. J. 2016, JPhCS, 728, 032008
Rathborne, J. M., Longmore, S. N., Jackson, J. M., et al. 2015, ApJ, 802, 125
Rickert, M., Yusef-Zadeh, F., & Ott, J. 2019, MNRAS, 482, 5349
Roberts, D. A., & Goss, W. M. 1993, ApJS, 86, 133
Robitaille, T., & Bressert, E. 2012, APLpy: Astronomical Plotting Library in Python v2.0, Astrophysics Source Code Library, ascl:1208.017
Rodríguez, L. F., & Zapata, L. A. 2013, ApJL, 767, L13
Sánchez-Monge, Á, Kurtz, S., Palau, A., et al. 2013, ApJ, 766, 114
Sewilo, M., Churchwell, E., Kurtz, S., Goss, W. M., & Hofner, P. 2004, ApJ, 605, 285
Tsuboi, M., Kitamura, Y., Miyoshi, M., et al. 2016, PASJ, 68, L7
Tsuboi, M., Kitamura, Y., Uehara, K., et al. 2017, ApJ, 842, 94
Tsujimoto, M., Hosokawa, T., Feigelson, E. D., Getman, K. V., & Broos, P. S. 2006, ApJ, 653, 409
van der Walt, D. J. 2014, A&A, 562, A68
Walker, D. L., Longmore, S. N., Bastian, N., et al. 2015, MNRAS, 449, 715
Walker, D. L., Longmore, S. N., Zhang, Q., et al. 2018, MNRAS, 474, 2373
Walsh, A. J., Breen, S. L., Britton, T., et al. 2011, MNRAS, 416, 1764
Wang, Q. D., Dong, H., Cotera, A., et al. 2010, MNRAS, 402, 895
Wang, Y., Bihr, S., Rugel, M., et al. 2018, A&A, 619, A124
Xu, Y., Li, J. J., Hachisuka, K., et al. 2008, A&A, 485, 729
Yusef-Zadeh, F., Hewitt, J. W., Arendt, R. G., et al. 2009, ApJ, 702, 178
Yusef-Zadeh, F., Hewitt, J. W., & Cotton, W. 2004, ApJS, 155, 421
Yusef-Zadeh, F., Lacy, J. H., Wardle, M., et al. 2010, ApJ, 725, 1429
Yusef-Zadeh, F., & Morris, M. 1987a, AJ, 94, 1178
Yusef-Zadeh, F., & Morris, M. 1987b, ApJ, 320, 545
Yusef-Zadeh, F., Morris, M., & Chance, D. 1984, Natur, 310, 557
Zhao, J.-H., Morris, M. R., & Goss, W. M. 2013, ApJ, 777, 146
Zhao, J.-H., Morris, M. R., & Goss, W. M. 2016, ApJ, 817, 171
Zhao, J.-H., Morris, M. R., Goss, W. M., & An, T. 2009, ApJ, 699, 186
Zhao, J.-H., & Wright, M. C. H. 2011, ApJ, 742, 50
Zhu, Z., Li, Z., & Morris, M. R. 2018, ApJS, 235, 26
Zoonematkermani, S., Helfand, D. J., Becker, R. H., White, R. L., & Perley, R. A. 1990, ApJS, 74, 181